

Cosmological constraints from a joint analysis of cosmic microwave background and large-scale structure

Cyrille Doux,^{1*} Mariana Penna-Lima,^{1,2,3} Sandro D. P. Vitenti,^{2,4,5}
Julien Tréguer,¹ Eric Aubourg,¹ and Ken Ganga¹

¹*APC, AstroParticule et Cosmologie, Université Paris Diderot, CNRS/IN2P3, CEA/Irfu, Observatoire de Paris, Sorbonne Paris Cité, 10, rue Alice Domon et Léonie Duquet, 75205 Paris Cedex 13, France*

²*Centro Brasileiro de Pesquisas Físicas, Rua Dr. Xavier Sigaud 150, CEP 22290-180, Rio de Janeiro, RJ, Brazil*

³*Laboratoire d'Annecy-le-Vieux de Physique des Particules (LAPP), Université Savoie Mont Blanc, CNRS/IN2P3, F-74941 Annecy, France*

⁴*Institut d'Astrophysique de Paris (GReCO), UMR 7095 CNRS, Sorbonne Universités, UPMC Univ. Paris 06, Institut Lagrange de Paris, 98 bis boulevard Arago, 75014 Paris, France*

⁵*Centre for Cosmology, Particle Physics and Phenomenology, Institute of Mathematics and Physics, Louvain University, 2 Chemin du Cyclotron, 1348 Louvain-la-Neuve, Belgium*

Accepted XXX. Received YYY; in original form ZZZ

ABSTRACT

The standard model of cosmology, Λ CDM, is the simplest model that matches the current observations, but relies on two hypothetical components, to wit, dark matter and dark energy. Future galaxy surveys and cosmic microwave background (CMB) experiments will independently shed light on these components, but a joint analysis that includes cross-correlations will be necessary to extract as much information as possible from the observations. In this paper, we aim at developing the methods needed to perform such an analysis, and test it on publicly available data sets. In particular, we use CMB temperature anisotropies and CMB lensing observations from Planck, and the spectroscopic galaxy and quasar samples of SDSS-III/BOSS. We build a likelihood to simultaneously analyse the auto and cross spectra of the CMB lensing and the galaxy overdensity maps before running Monte-Carlo Markov Chains (MCMC) to assess the constraining power of the combined analysis. We then add CMB temperature information and run MCMCs to test the Λ CDM model. We present constraints on cosmological parameters and galaxy biases, and demonstrate that the joint analysis can additionally constrain the mass of neutrinos as well as the dark energy equation of state. Finally, we discuss several difficulties regarding the analysis itself and the theoretical precision of the models, which will require additional work to properly analyse the observations of the next generation of cosmological experiments.

Key words: cosmological parameters – cosmic background radiation – large-scale structure of Universe – dark energy

1 INTRODUCTION

The large amount of cosmological data collected in the last few decades has been shedding light on the content of the Universe. Assuming General Relativity (GR) and the cosmological principle, the combination of different cosmological probes, such as type Ia supernovæ, primary anisotropies of the cosmic microwave background (CMB), and large-scale structure (LSS) information, among others, indicates that the universe is almost flat, is dominated today by a dark energy (DE) component driving the current accelerated ex-

pansion phase of the Universe, and has some form of cold dark matter (CDM) in addition to baryons and radiation (Planck Collaboration et al. 2016e). The flat Λ CDM model is currently the simplest model compatible with the data of these combined probes.

We are reaching a precision era in cosmology and we may be able, in the near future, to distinguish between various cosmological models and achieve a better understanding of the fundamental nature of the DE and DM components. Upcoming photometric and spectroscopic galaxy surveys such as the Large Synoptic Survey Telescope (LSST, LSST Science Collaborations and LSST Project et al. 2009), Euclid (Refregier et al. 2010), the Wide Field Infrared Survey Tele-

* E-mail: cdoux@apc.in2p3.fr

scope (WFIRST, Spergel et al. 2013) and the Dark Energy Spectroscopic Instrument (DESI, Levi et al. 2013; Schlegel et al. 2009), aim at shedding light on those questions by probing the matter density field with ground-breaking precision. They will provide the data necessary for a deeper investigation of Λ CDM and its competitors, hopefully allowing us to distinguish them. Additionally, secondary anisotropies of the CMB due to gravitational lensing, the thermal (tSZ) and kinetic (kSZ) Sunyaev-Zeldovich effects and the integrated Sachs-Wolfe (ISW) effect encode much information about dark matter and dark energy (Peiris & Spergel 2000b). Therefore, future CMB experiments, such as the Simons Observatory (Suzuki et al. 2016) and the Stage-IV CMB experiment (CMB-S4, Abazajian et al. 2016), will provide valuable complementary observations.

While various observations from multiple telescopes will provide exquisite and hopefully complementary data sets (Jain et al. 2015), they will all observe the same sky, *i.e.* the same underlying matter density field. Therefore, the observables they will measure are potentially statistically correlated. In this context, the cross-correlation between cosmological probes of different experiments yields new information, that is less prone to biases since different experiments are assumed to have uncorrelated noise and independent systematic effects. This correlation needs to be taken into account in the joint statistical analysis of multiple data sets in order to properly extract as much information as possible from it, without underestimating error bars on cosmological parameters (Rhodes et al. 2015). If this makes the analysis more demanding, the outcome is expected to provide stronger constraints on *e.g.* dark energy, dark matter, the mass of neutrinos (Pearson & Zahn 2014) or primordial non-gaussianities (Takeuchi et al. 2012).

Initially, some of the best-explored cross-correlation information was that from CMB and galaxy surveys in order to measure the ISW signal (Crittenden & Turok 1996; Boughn et al. 1998; Fosalba et al. 2003; Cabré et al. 2006; Moura-Santos et al. 2016). But over the last decade, many different cross-correlation signals have been detected, combining various probes: the CMB anisotropies themselves, the CMB lensing potential, galaxy clustering, cosmic shear from the observations of galaxy weak lensing, etc. In particular, correlations of the gravitational lensing of the CMB with positions of galaxies (Hirata et al. 2008; Ho et al. 2008; Bleem et al. 2012; Sherwin et al. 2012; Geach et al. 2013; Bianchini et al. 2015; Fornengo et al. 2015; Allison et al. 2015; Baxter et al. 2016; Giannantonio et al. 2016; Harnois-Déraps et al. 2016; Bianchini et al. 2016) and lensing of galaxies (Hand et al. 2015; Kirk et al. 2016) have been measured for various surveys. These measurements can provide unbiased estimates of galaxy biases, which encode the link between baryonic and dark matter, or the shear multiplicative bias (Vallinotto 2012; Liu et al. 2016; Schaan et al. 2016a). Finally, they have also been used to detect new signals, *e.g.* the first detection of CMB lensing by cross-correlation with the NRAO VLA sky survey (Smith et al. 2007), the tSZ effect (Hajian et al. 2013; Hill & Spergel 2014), the kSZ effect (Hand et al. 2012; Schaan et al. 2016b), and the position-dependent Lyman- α power spectrum (Doux et al. 2016).

Pearson & Zahn (2014) forecast constraints on the neutrino mass, DE density and the reionization optical depth from future, fourth-generation CMB experiments and galaxy

surveys such as LSST and Euclid. Kwan et al. (2017) used the Dark Energy Survey Science Verification data to obtain cosmological constraints considering the cross-correlation between the angular clustering of red galaxies and the weak gravitational lensing of background galaxies. While offering great confirmation of the current picture, the cross-correlation signals have not yet been systematically used in the estimation of cosmological parameters. This is precisely what we aim to do in this work.

To this end, we build a joint likelihood of the CMB lensing and the contrast density of galaxies using auto and cross spectra of these fields. In particular we use the Planck 2015 lensing map (Planck Collaboration et al. 2016g) and the three spectroscopic samples of the Sloan Digital Sky Survey and its Baryon Oscillation Spectroscopic Survey (SDSS-III/BOSS, Dawson et al. 2013; Reid et al. 2016; Pâris et al. 2017); that is LOWZ, CMASS and the uniform quasar sample. We then run a Markov Chain Monte-Carlo (MCMC) analysis to extract constraints on cosmological parameters. It is worth mentioning that we developed a general framework in the Numerical Cosmology library (NumCosmo, Dias Pinto Vitenti & Penna-Lima 2014) to compute the auto and cross correlations for, in principle, an arbitrary number of cosmological probes. We complete our work by performing a joint analysis with CMB temperature (Planck Collaboration et al. 2016d,f) and demonstrate the performance of such an analysis to constrain the Λ CDM model and extensions of it, fitting the six base parameters (H_0 , ω_b , ω_c , A_s , n_s and z_{re}) as well as the mass of neutrinos, m_ν , and the DE equation of state, $w = p/\rho$.

The paper outline is as follows. In Section 2, we develop the theoretical formalism, considering the Limber formula, to compute the pseudo angular power spectra of CMB lensing and galaxy overdensities. In Section 3, we describe the data used in this work and prepare the galaxy and quasar density maps. In Section 4, we develop the estimators and construct the likelihood used in this work, and then we perform the validation and null tests. In Section 5, we detail the results of the statistical analyses and present constraints on cosmological parameters. Finally, we draw conclusions in Section 6.

2 THEORETICAL BACKGROUND

2.1 Cross-correlation

The matter distribution of the Universe is traced by cosmological probes such as galaxies, quasars (QSOs) and CMB lensing, among others. Their projected random fields on the observed direction $\hat{\mathbf{n}}$ can be written as

$$A(\hat{\mathbf{n}}) = \int_0^\infty dz W^A(z) \delta(\chi(z)\hat{\mathbf{n}}, z), \quad (1)$$

where $W^A(z)$ is the kernel function of an observable A (kernels of the probes used in this work are plotted in Figure 1), $\delta = \delta\rho/\rho$ is the matter density contrast, ρ is the matter density, and $\chi(z)$ is the comoving distance at redshift z . The fields $A(\hat{\mathbf{n}})$ and $B(\hat{\mathbf{n}})$, associated with galaxy or QSO density contrast and CMB lensing, are assumed to be statistically homogeneous and isotropic. Therefore the correlation function $\langle A(\hat{\mathbf{n}})B^*(\hat{\mathbf{n}}') \rangle$ only depends on $\hat{\mathbf{n}} \cdot \hat{\mathbf{n}}'$ and can be

expanded as

$$\langle A(\hat{\mathbf{n}})B^*(\hat{\mathbf{n}}') \rangle = \sum_{\ell=0}^{\infty} \frac{(2\ell+1)}{4\pi} P_{\ell}(\hat{\mathbf{n}} \cdot \hat{\mathbf{n}}') C_{\ell}^{AB} \quad (2)$$

where P_{ℓ} are the Legendre polynomials, which defines the angular power spectrum C_{ℓ}^{AB} .¹

Using the inverse Fourier transform of the matter density field in eq. (1) and substituting it into eq. (2), we obtain

$$C_{\ell}^{AB} = \int dz W^A(z) \int dz' W^B(z') \times \int dk \frac{2}{\pi} k^2 P(k, z, z') j_{\ell}(k\chi(z)) j_{\ell}(k\chi(z')), \quad (3)$$

where $P(k, z, z')$ is the matter power spectrum and j_{ℓ} are the spherical Bessel functions. In this work, we adopt the Limber approximation (Limber 1953; LoVerde & Afshordi 2008) and assume that spatial sections of the Universe are flat², thus eq. (3) becomes

$$C_{\ell}^{AB} = \int_0^{z_*} dz \frac{H(z)}{c\chi^2(z)} W^A(z) W^B(z) P\left(k = \frac{\ell + 1/2}{\chi(z)}, z\right) \quad (4)$$

where c is the speed of light and $H(z)$ is the Hubble parameter. This approximation is valid when $P(k, z, z')$ varies slowly in comparison with the Bessel functions. In particular, the CMB lensing spectra are accurate for $\ell > 10$ (Lesgourgues & Tram 2014). The selection functions of galaxies and quasars are wider than the largest scales probed³ for the spectroscopic tracers used here. Therefore, we can safely make use of this approximation to compute theoretical power spectra, which are integrals of the matter power spectrum weighted by the kernel functions corresponding to each observable. We detail this in the following sections.

2.2 Cosmic microwave background gravitational lensing

The trajectories of the CMB photons are disturbed by the matter distribution such that, among other effects, the observed anisotropies of the temperature field in a direction $\hat{\mathbf{n}}$ correspond to the unlensed field deflected by α , i.e., $\bar{T}(\hat{\mathbf{n}}) = T(\hat{\mathbf{n}} + \alpha)$ (Lewis & Challinor 2006). Assuming the small-angle Born approximation, α comprises the variations in the gravitational potential Ψ along the line of sight from today's observer to the last scattering surface at redshift z_* , i.e.,

$$\alpha = -2 \int_0^{z_*} dz \frac{c}{H(z)} \frac{\chi(z_*) - \chi(z)}{\chi(z)\chi(z_*)} \nabla_{\hat{\mathbf{n}}} \Psi(\chi\hat{\mathbf{n}}, z). \quad (5)$$

¹ Expanding the fields in spherical harmonics, $A(\hat{\mathbf{n}}) = \sum_{\ell m} A_{\ell m} Y_{\ell m}(\hat{\mathbf{n}})$, this implies that $\langle A_{\ell m} B_{\ell' m'} \rangle = C_{\ell}^{AB} \delta_{\ell \ell'} \delta_{m m'}$.

² It is worth noting that Limber approximation can be also applied for curved space universe, see Lesgourgues & Tram (2014), for instance.

³ For a given sample, the largest scale probed is $\chi_{\max} \sim \pi/k_{\min}$ with $k_{\min} = (\ell_{\min} + 1/2)/\chi(z_{\text{eff}})$, where $\chi(z_{\text{eff}})$ is the comoving distance at the mean redshift of the sample and $\ell_{\min} = 20$, see Section 3. For LOWZ, CMASS and QSO, these scales are of order 110, 220 and 630 Mpc/h, while the selection functions have widths of order 1080, 860 and 970 Mpc/h.

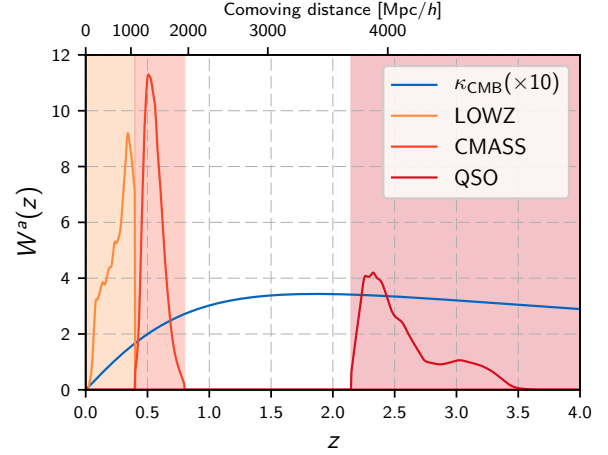


Figure 1. Kernel functions $W^A(z)$ of the observables used for cross-correlation as defined in equations (6) and (8). For the LOWZ, CMASS and QSO samples, $W^g(z)$ reflects the redshift distribution (multiplied by the bias). The background colours correspond to the extent of the redshift distributions of the three samples. The CMB lensing kernel (multiplied by 10 on this plot for visibility) is very broad and peaks around $z \approx 2$.

The remapping of the CMB temperature anisotropies due to the weak lensing effect is described at lowest order by the convergence $\kappa_{\text{CMB}} = -\frac{1}{2} \nabla_{\hat{\mathbf{n}}}^2 \alpha$. Given that on small angular scales $\nabla_{\hat{\mathbf{n}}}^2 \simeq \nabla^2$ (Jain et al. 2000) and using the Poisson equation and eq. (1), we obtain the CMB convergence kernel

$$W^{\kappa_{\text{CMB}}}(z) = \frac{3}{2} \frac{\Omega_m H_0^2}{c} \frac{(1+z)}{H(z)} \chi(z) \frac{\chi(z_*) - \chi(z)}{\chi(z_*)}, \quad (6)$$

where Ω_m and H_0 are the present-day matter density and Hubble constant, respectively.

2.3 Large-scale structure tracers

Similarly to the CMB lensing, the galaxy or quasar overdensity in the direction $\hat{\mathbf{n}}$ is a function of $\delta(\chi\hat{\mathbf{n}}, z)$, namely

$$g(\hat{\mathbf{n}}) = \int_0^\infty dz W^g(z) \delta(\chi\hat{\mathbf{n}}, z). \quad (7)$$

The kernel $W^g(z)$ is given by (Peiris & Spergel 2000a; Bonvin & Durrer 2011)

$$W^g(z) = b(z) \frac{dn}{dz} + \frac{3\Omega_m}{2c} \frac{H_0^2}{H(z)} (1+z) \chi(z) (5s-2) g(z) \quad (8)$$

where

$$g(z) = \int_z^{z_*} dz' \left(1 - \frac{\chi(z)}{\chi(z')} \right) \frac{dn}{dz'}. \quad (9)$$

The function $b(z)$ is the linear bias relating the galaxy overdensity to the matter overdensity at large scales as $\delta_g(\chi\hat{\mathbf{n}}, z) = b(z) \delta(\chi\hat{\mathbf{n}}, z)$, and dn/dz is the normalised redshift distribution of the tracers, which also contains the survey selection function. The second term in eq. (8) is due to the effects of gravitational lensing, with two opposing contributions – the dilation of the apparent surveyed volume

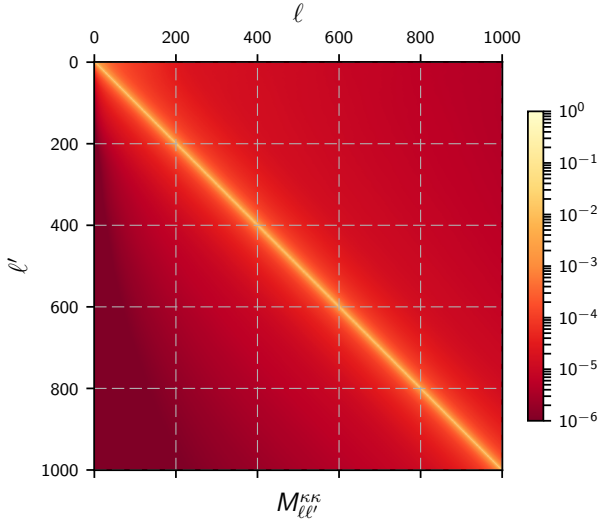


Figure 2. Mixing matrix of the CMB lensing auto power spectrum (see the mask in Figure 3a) relating the full-sky power spectrum $C_{\ell}^{\kappa\text{CMB}\kappa\text{CMB}}$ to the pseudo spectrum $\tilde{C}_{\ell}^{\kappa\text{CMB}\kappa\text{CMB}}$ as in eq. (11). The matrix elements are strongly dominated by the diagonal terms and the coupling between modes is given by off-diagonal elements. The other mixing matrices are qualitatively very similar.

and the magnification bias effect for flux-limited samples⁴, where

$$s = \left. \frac{d \log N(< m)}{dm} \right|_{m=m_{\max}}. \quad (10)$$

$N(< m)$ denotes the cumulative count of objects with a magnitude smaller than m and the derivative is estimated at the faint end of the catalog (Scranton et al. (2005); Hui et al. (2007)). This term can be neglected when using LOWZ and CMASS samples, but it is relevant for quasars (Chisari & Dvorkin 2013). Following Scranton et al. (2005), we use $s_{\text{qso}} = 0.2$ throughout this analysis.

2.4 Pseudo spectra

Many galaxy and CMB surveys cover only a fraction of the sky due to, for example, the limited field of view or galactic contamination, among others. In order to properly account for the partial sky coverage in the calculation of the angular power spectra, we define the mask function associated with the field $A(\hat{\mathbf{n}})$ as being $\mathcal{W}^A(\hat{\mathbf{n}})$ with value 1 if the direction $\hat{\mathbf{n}}$ lies in the observed region, and 0 otherwise.

The cross-pseudo spectrum of observables A and B is thus defined as the cross spectrum of the cut-sky fields $\tilde{A}(\hat{\mathbf{n}}) = \mathcal{W}^A(\hat{\mathbf{n}})A(\hat{\mathbf{n}})$ and $\tilde{B}(\hat{\mathbf{n}}) = \mathcal{W}^B(\hat{\mathbf{n}})B(\hat{\mathbf{n}})$, and its expected value can be related to the (true) full-sky cross spectrum in eq. (3) by (Brown et al. 2005)

$$\langle \tilde{C}_{\ell}^{AB} \rangle = \sum_{\ell'} M_{\ell\ell'}^{AB} C_{\ell'}^{AB}, \quad (11)$$

⁴ Lensed galaxies may appear brighter than they are and pass the luminosity threshold.

where $M_{\ell\ell'}^{AB}$ is the mixing matrix which is given in terms of the Wigner-3j symbols

$$M_{\ell\ell'}^{AB} = \frac{2\ell+1}{4\pi} \sum_{\ell''} (2\ell''+1) \mathcal{W}_{\ell''}^{AB} \begin{pmatrix} \ell & \ell' & \ell'' \\ 0 & 0 & 0 \end{pmatrix}^2. \quad (12)$$

The cross spectra of the masks are

$$\mathcal{W}_{\ell\ell'}^{AB} = \frac{1}{2\ell''+1} \sum_m w_{\ell''m}^A (w_{\ell''m}^B)^*, \quad (13)$$

where

$$w_{\ell m}^A = \int d\hat{\mathbf{n}} \mathcal{W}^A(\hat{\mathbf{n}}) Y_{\ell m}^*. \quad (14)$$

The mixing matrix introduces a scaling factor equal to $(f_{\text{sky}}^A f_{\text{sky}}^B)^{1/2}$, i.e., the geometric mean of the observed sky fractions for the observables A and B , respectively, since the form of the masked function is constant (Hivon et al. 2002). It also couples the multipoles ℓ and ℓ' , that would be otherwise uncorrelated, especially at large scales. It is computed analytically for each pair of observables (see Figure 2).

3 DATA

3.1 Planck data

3.1.1 CMB temperature data

Planck⁵ (Planck Collaboration et al. 2016a), the fourth satellite to survey the Cosmic Microwave Background over the full sky, was launched on May 14th, 2009. Its scientific payload comprised two instruments: the Low Frequency Instrument (Mandolesi et al. 2010), which observed for four years in bands at 30, 44 and 70 GHz, and the High Frequency Instrument (Lamarre et al. 2010), which observed for almost two-and-a-half years in bands at 100, 143, 217, 353, 545 and 857 GHz.

In this work, we use both the primordial CMB anisotropy likelihood codes (Plik for the high multipoles, $\ell \geq 30$, and Commander for low multipoles, $\ell < 30$, see details in Planck Collaboration et al. 2016d) and the CMB lensing maps (Planck Collaboration et al. 2016g) from Planck. Both these products are based largely on the Spectral Matching Independent Component Analysis (SMICA) maps of the temperature of the CMB.

3.1.2 CMB lensing data

We use the CMB lensing convergence map from the Planck 2015 data release (Planck Collaboration et al. 2016g). The Planck Collaboration provides the convergence map⁶ in the Healpix⁷ (Górski et al. 2005) format, with resolution parameter $N_{\text{side}} = 2048$, and the corresponding binary mask, with a sky fraction $f_{\text{sky}} = 0.67$. Lensing potential maps were reconstructed using the temperature and polarisation maps forming five quadratic estimators $\hat{\phi}^{TT}$, $\hat{\phi}^{TE}$, $\hat{\phi}^{EE}$, $\hat{\phi}^{EB}$ and

⁵ <http://sci.esa.int/planck/>

⁶ The convergence map and mask files are publicly available at <http://pla.esac.esa.int/pla/>.

⁷ <http://healpix.jpl.nasa.gov/>

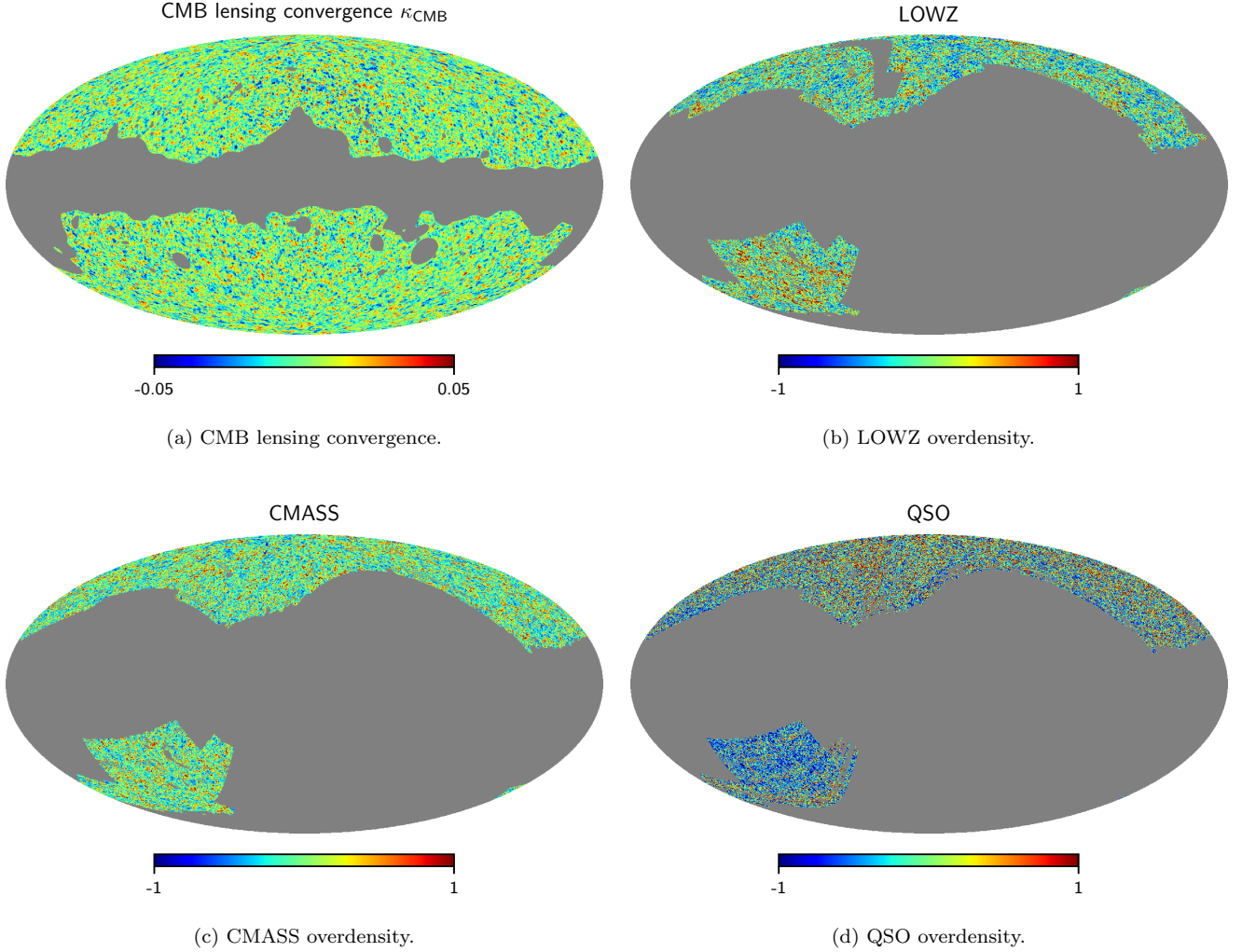


Figure 3. Planck CMB lensing convergence and BOSS galaxy and quasar overdensity maps in galactic coordinates. The auto and cross spectra of these maps are used in this work. Grey areas correspond to the masked areas near the galactic plane. The lensing map has been Wiener-filtered and the overdensity maps have been smoothed on one degree scale for visualisation purposes only.

$\hat{\phi}^{TB}$, combined into a minimum-variance estimator (for details, see Planck Collaboration et al. 2016g). The convergence map is shown in Figure 3a.

3.2 SDSS-III/BOSS data

3.2.1 Luminous Red Galaxies: LOWZ & CMASS

The spectroscopic galaxy sample of the Baryon Oscillations Spectroscopic Survey (BOSS, Dawson et al. 2013), which is part of the Sloan Digital Sky Survey III (SDSS-III), consists of two catalogs named LOWZ and CMASS. They are extensively described in Reid et al. (2016) and we only summarize relevant information in this section.

LOWZ contains Luminous Red Galaxies (LRG) at low redshift ($z \lesssim 0.4$), and it aims at a constant number density of about $\bar{n} \sim 3 \times 10^{-4} h^3 \text{Mpc}^{-3}$ over the redshift range [0.1, 0.4]. This is done using a redshift dependent magnitude cut. In this work, we use the twelfth data release (DR12) and select galaxies in the range 0-0.4, which contains 383876

galaxies. The CMASS sample contains galaxies at higher redshifts $0.4 \lesssim z \lesssim 0.8$ with a constant stellar mass in this redshift range. The twelfth data release contains 849637 galaxies in the redshift range 0.4-0.8 used in this work. The normalised redshift distributions of the two samples are shown on Figure 1 (multiplied by their respective biases).

BOSS's spectroscopic fibres are plugged into tiles of diameter 3° to observe predetermined targets. The combined footprints of all tiles can be decomposed into non-overlapping sky sectors. Because of the finite size of fibres, galaxies closer than $62''$ may not be observed even after multiple observations of the same field. The pipeline may also fail in determining the redshift of some galaxies (especially the faintest ones). Therefore, for each sector i , the completeness is defined as the ratio of observed galaxies with a measured redshift to the number of targets lying in that same sector

$$C_i = \frac{N_{\text{obs},i}}{N_{\text{targ},i}}. \quad (15)$$

The completeness maps are defined in the **Mangle** software⁸ format and are converted to **Healpix** maps with resolution parameter $N_{\text{side}} = 2048$. The mask functions of the galaxy samples are obtained by assigning 1 to pixels where the completeness is above 75% and then removing small areas that were vetoed for bad photometry, bright objects and stars and instrumental constraints, such as fibre centerposts and fibre collisions.

In order to correct for completeness, each galaxy is thus assigned a weight

$$w_{\text{tot}} = w_{\text{star}} w_{\text{seeing}} (w_{\text{cp}} + w_{\text{noz}} - 1), \quad (16)$$

where w_{star} and w_{seeing} correct for non-cosmological fluctuation in the target selection due to stellar density (only for the CMASS sample) and atmospheric seeing, w_{cp} corrects for fibre collisions and w_{noz} corrects for redshift failures.

3.2.2 Quasars

The selection function (over the sky) of the full quasar sample of BOSS is not uniform due to the observing strategy, hence we shall use the so-called CORE sample which contains QSOs with redshift $z \geq 2.15$ that were uniformly selected by the XDQSO algorithm (Bovy et al. 2011). There are 94971 quasars in the CORE sample of DR12 within this redshift range. The completeness is computed using the BOSSQS-SOMASK software⁹ from Eftekharzadeh et al. (2015) and is then combined with the veto mask to build the mask of the quasar density map.

3.2.3 Building the maps

For the LOWZ and CMASS samples, we build **Healpix** maps with resolution parameter $N_{\text{side}} = 2048$, where for each pixel p ,

$$\delta_p = \frac{N_p}{\bar{N}} - 1. \quad (17)$$

$N_p = \sum_{i \in p} w_i$ is the number of galaxies in pixel p counted with their weights and $\bar{N} = \frac{1}{N_{\text{pix}}} \sum_{p=1}^{N_{\text{pix}}} N_p$ is the mean pixel count (where the sum runs only on pixels in the observed area, *i.e.* where the mask function is equal to 1).

For the quasars, there is no weight provided in the BOSS DR12 catalog and the density map is computed as

$$\delta_p = \frac{N_p}{\bar{N}/C_{s(p)}} - 1, \quad (18)$$

where this time N_p denotes the number of QSOs lying in pixel p and \bar{N} denotes the mean pixel count in the observed area. The denominator is up-weighted by the completeness $C_{s(p)}$ of the sector $s(p)$ where the pixel p lies.

The angular densities of the samples are $\bar{n}_{\text{LOWZ}} = 150 \times 10^3 \text{ steradian}^{-1}$, $\bar{n}_{\text{CMASS}} = 300 \times 10^3 \text{ steradian}^{-1}$ and $\bar{n}_{\text{QSO}} = 36 \times 10^3 \text{ steradian}^{-1}$. The maps of the estimated overdensity for the three samples are shown in Figures 3b, 3c and 3d.

3.3 CMB lensing–large-scale structure correlations data

In this work, we will use, in addition to CMB temperature data, auto and cross spectra of CMB lensing from Planck and spectroscopic tracers from BOSS. More precisely, we will use the auto-pseudo spectra of the CMB lensing map κ_{CMB} and of the density contrast maps of the LOWZ and CMASS samples. We also use the pseudo-cross-spectra of the CMB lensing map with the three LSS tracers. The collection of these six spectra (shown in Figure 4) will henceforth be referred to as “CMB lensing-LSS correlations”, and denoted CMB lensing \otimes LSS in the figures.

We do not use the auto spectrum of the QSO map because it is completely shot-noise-dominated in multipole space. We do not use the galaxy cross spectra because their redshift ranges do not overlap and the cross spectra should therefore be zero in the Limber approximation (which we check in the next section).

We use multipoles in the range $[20, 500]$ for all auto- and cross-pseudo spectra. The small-scale limit $\ell_{\text{max}} = 500$ is determined by the CMB lensing resolution – 90% of the lensing signal is in the range $[40, 400]$ – and the shot-noise of the galaxy/quasar auto spectra – \tilde{C}_ℓ^{gg} becomes noise dominated for all samples (CMASS being the limiting one) for $\ell \geq \ell_{\text{max}}$. The large-scale limit is fixed at $\ell_{\text{min}} = 20$ for of the following reasons:

- Partial sky coverage limits the number of large-scale modes accessible.
- CMB lensing is measured from $\ell_{\text{min}} = 8$.
- Field-dependent observing conditions during the SDSS photometric and spectroscopic surveys could contaminate the measurement of the overdensity fields on large-scales.¹⁰

The six observed pseudo spectra are shown in Figure 4 together with theoretical curves for our best-fit biases ($b_{\text{LOWZ}} = 1.871 \pm 0.025$, $b_{\text{CMASS}} = 2.095 \pm 0.022$ and $b_{\text{QSO}} = 2.21 \pm 0.44$) and with fixed cosmology.¹¹ We report detections for the CMB lensing-galaxy density cross-correlations of 4.7 σ , 13.9 σ and 10.6 σ for LOWZ, CMASS and QSO, respectively.

4 METHODOLOGY

4.1 Likelihood

4.1.1 Pseudo spectra estimator

Pseudo spherical harmonic coefficients $\tilde{A}_{\ell m}$ and $\tilde{B}_{\ell m}$ (for $A, B \in \{\text{LOWZ}, \text{CMASS}, \text{QSO}, \kappa_{\text{CMB}}\}$) of the four maps are estimated with the **map2alm** function of **Healpix** and

⁸ See <http://space.mit.edu/~molly/mangle/>.

⁹ See <http://faraday.uwyo.edu/~admyers/bossqsomask/>.

¹⁰ The size of the BOSS plates (3°) correspond to a multipole of $\ell \sim \pi/\theta = 60$.

¹¹ Parameters’ values are fixed at the best-fit cosmology for Planck “TT,TE,EE+lowP+lensing+ext” (Planck Collaboration et al. 2016f) for the flat Λ CDM model with a mass of neutrinos $m_\nu = 0.06 \text{ eV}$.

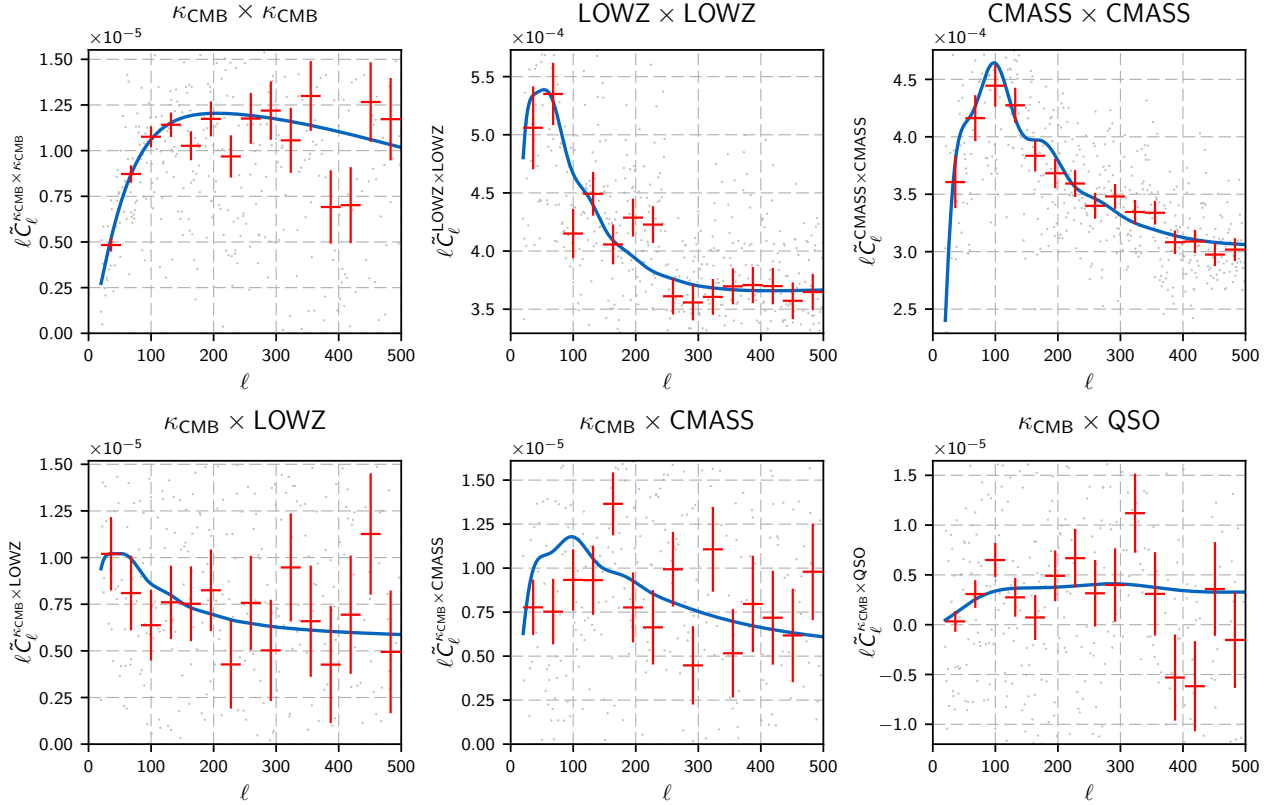


Figure 4. Auto- and cross-pseudo spectra used in this paper. Observed spectra are represented by the light grey points in the multipole range 20 – 500, and binned as red error bars (only for visualisation). The theoretical curves, for best-fit biases and fixed Planck cosmology, are represented by the solid blue curves. Pseudo spectra are multiplied by ℓ to help visualise features of the theoretical power spectra, especially the wiggling related to baryon acoustic oscillations (and the covariance matrix is modified accordingly).

summed to give an estimator of the pseudo spectra

$$\hat{C}_\ell^{AB} = \frac{1}{2\ell+1} \sum_{m=-\ell}^{m=+\ell} \tilde{A}_{\ell m} \tilde{B}_{\ell m}^*. \quad (19)$$

These pseudo spectra have a noise contribution and an expectation value

$$\langle \hat{C}_\ell^{AB} \rangle = \sum_{\ell'} M_{\ell\ell'}^{AB} C_{\ell'}^{AB} + \delta_{AB} \tilde{N}_\ell^A \quad (20)$$

where \tilde{N}_ℓ^A is the noise pseudo-spectrum of the measured field $A(\hat{n})$, which needs to be subtracted. It is assumed here that different observables have uncorrelated noise, *i.e.* that noise cross spectra are null (for both full-sky and pseudo).

In principle, noise pseudo spectra can be computed using the mixing matrix and eq. (11).

$$\tilde{N}_\ell^A = \sum_{\ell'} M_{\ell\ell'}^{AA} N_{\ell'}^A. \quad (21)$$

However, the sum over ℓ' runs from 0 to infinity, so, in practice, it has to be cut at some maximum multipole ℓ_{\max} . But convergence is not guaranteed, since noise spectra are increasing functions of ℓ (they are quasi-constant for galaxies and grow like $\sim \ell^2$ for CMB lensing). Therefore, we used instead simulated noise maps for both CMB lensing and galaxies.

For CMB lensing, we used the 100 simulated lensing reconstruction maps provided by the Planck Legacy Archive.¹² Given a known, full-sky, input convergence map (to be masked) and a masked, reconstructed convergence map, one can compute the difference of the pseudo spectra in order to obtain an estimate of the noise pseudo power spectrum \tilde{N}_ℓ^κ , which is then averaged over realisations of the simulation.

For the galaxy catalogs, the full-sky shot noise spectrum is $N_\ell = 1/\bar{n}$, where \bar{n} is the angular density of objects (weighted and expressed in steradian⁻¹). In order to estimate the pseudo spectra, random maps with a pure Poisson distribution of appropriate density are generated and then masked. The pseudo spectra of 100 maps are averaged to get an estimate of the pseudo noise spectra \tilde{N}_ℓ^g . However, weights slightly increase the noise level, which is henceforth assumed to be of the form $\tilde{N}_\ell^g + a^g$, where a^g is a small nuisance parameter to be marginalised over during the analysis, and that we found to be one order of magnitude smaller than \tilde{N}_ℓ^g .

Our estimator thus reads

$$\hat{C}_\ell^{AB} = \frac{1}{2\ell+1} \sum_{m=-\ell}^{m=+\ell} \tilde{A}_{\ell m} \tilde{B}_{\ell m}^* - \delta_{AB} \frac{1}{N_{\text{sim}}} \sum_{i=1}^{N_{\text{sim}}} \hat{N}_\ell^{A,i}, \quad (22)$$

¹² See <http://pla.esac.esa.int/pla/>.

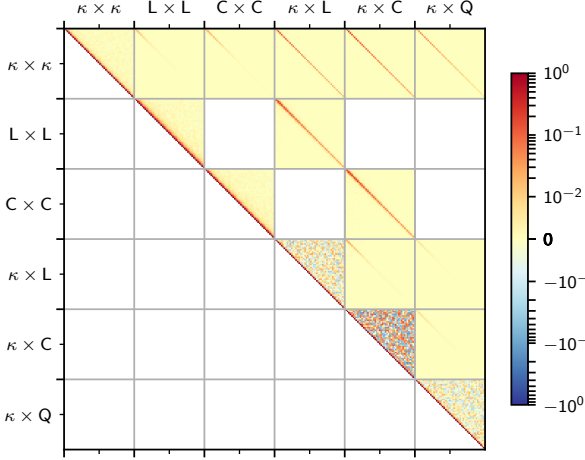


Figure 5. Full covariance matrix (normalised to unit diagonal) of the CMB lensing-LSS correlations computed from eq. (23) in symmetric logarithmic scale. It is divided in blocks corresponding to the six angular spectra: κ , L, C and Q correspond to respectively κ_{CMB} , LOWZ, CMASS and QSO. Note the (small) numerical noise in the variance blocks of the cross power spectra from the \mathbf{X}/\mathbf{Y} matrices. Only the upper part is displayed. The white blocks in the upper parts correspond to non-correlated spectra.

where $\hat{N}_{\ell}^{A,i}$ is the estimated pseudo-noise spectrum of simulation number i . The pseudo spectra used in this work are shown in Figure 4.

4.1.2 Covariance matrix and likelihood

The covariance matrix of the pseudo spectra is computed using an extension of Efstathiou’s symmetrisation approximation (Efstathiou 2004) following Brown et al. (2005) and is given by

$$\text{Cov}(\tilde{C}_{\ell}^{AB}, \tilde{C}_{\ell'}^{CD}) = \sqrt{D_{\ell}^{AD} D_{\ell'}^{AD} D_{\ell}^{BC} D_{\ell'}^{BC} \mathbf{X}_{\ell\ell'}^{ABCD}} + \sqrt{D_{\ell}^{AC} D_{\ell'}^{AC} D_{\ell}^{BD} D_{\ell'}^{BD} \mathbf{Y}_{\ell\ell'}^{ABCD}} \quad (23)$$

with

$$D_{\ell}^{AB} = \begin{cases} C_{\ell}^{AB} & \text{if } A \neq B \\ C_{\ell}^{AA} + N_{\ell}^A & \text{if } A = B \end{cases}, \quad (24)$$

where C_{ℓ}^{AB} and N_{ℓ}^A are the full-sky theoretical and noise spectra. $\mathbf{X}_{\ell\ell'}^{abcd}$ and $\mathbf{Y}_{\ell\ell'}^{abcd}$ are two matrices depending only on the masks of observables A, B, C, D , determined to arbitrary precision by a Monte-Carlo (MC) simulation (see Appendix A for more details). The covariance matrix (estimated for a fiducial cosmology) is shown in Figure 5.

A Gaussian likelihood is used for the stacked pseudo spectra vector

$$\mathcal{L}(\tilde{C}_{\ell}^{\text{obs}} | b_g, \Theta_{\text{cosmo}}) = \frac{1}{(2\pi)^{n/2} |\mathbf{Cov}|^{1/2}} e^{-\chi^2/2}, \quad (25)$$

where

$$\chi^2 = (\tilde{C}^{\text{obs}} - \tilde{C}^{\text{th}})^T [\mathbf{Cov}]^{-1} (\tilde{C}^{\text{obs}} - \tilde{C}^{\text{th}}), \quad (26)$$

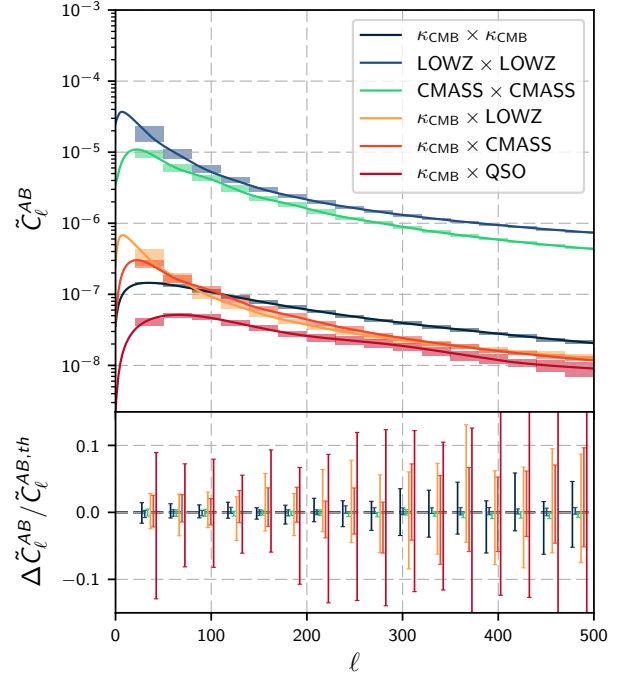


Figure 6. Validation of the pseudo spectrum estimator: the upper plot shows in solid line the theoretical pseudo spectra, computed using full-sky spectra and mixing matrices as in eq. (11). Boxes show the mean of the simulated pseudo spectra and its spread for 1000 realisations, binned for visualisation. The lower plots shows the relative error. All spectra are consistent with the theoretical expectations in the multipole range used for this work.

\tilde{C}^{obs} is the stacked vector of observed pseudo spectra (see Figure 4) and \tilde{C}^{th} is the stacked vector of theoretical pseudo spectra computed from the Limber approximation (see eq. (4)) and multiplied by the mixing matrices. The covariance matrix \mathbf{Cov} is that of the stacked vector as defined in eq. (23) and is shown in Figure 5.

4.2 Validation

In this section, we perform validation tests for the pseudo spectrum estimator, the covariance matrix and the statistical pipeline.

In order to validate the pseudo spectrum estimator and the semi-analytical expression of the covariance matrix given in eq. (23), we generate 1000 sets of four correlated full-sky maps with appropriate auto and cross spectra (for $\{\text{LOWZ}, \text{CMASS}, \text{QSO}, \kappa_{\text{CMB}}\}$) computed using eq. (4). These maps are then added realistic noise and are masked as follows: for each lensing convergence map, we add an uncorrelated Gaussian noise with spectrum N_{ℓ}^{κ} given by the approximate spectrum delivered by the Planck Legacy Archive, which is precise enough for the covariance validation. For each galaxy density map, we also need to simulate Poisson sampling. To do so, we generate a map where the value in pixel p is a Poisson random variable of mean λ_p , i.e.,

$$n_p \sim \text{Poisson}(\lambda_p) \quad \text{with} \quad \lambda_p = \bar{N}(1 + \delta_p), \quad (27)$$

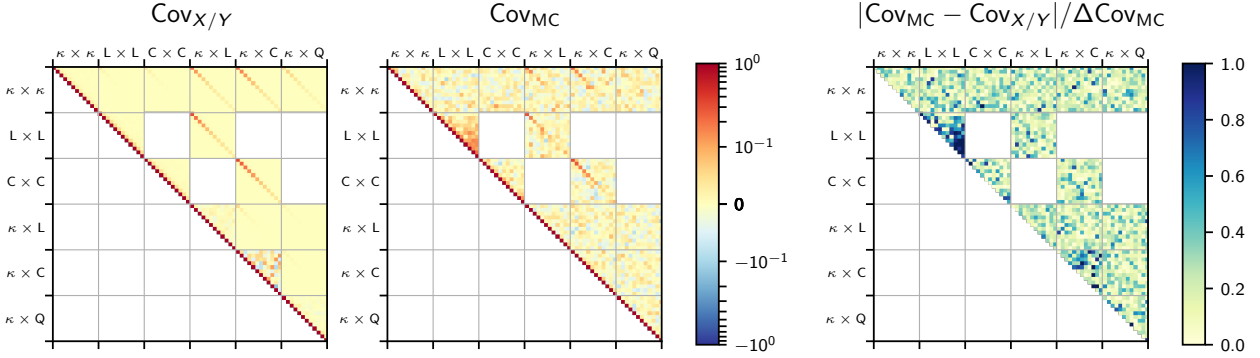


Figure 7. Validation of the covariance matrix. On the left panel, the covariance matrix used in the analysis from eq. (23), denoted $\text{Cov}_{X/Y}$; on the middle panel, the empirical covariance matrix of 1000 simulated stacked pseudo spectra, denoted Cov_{MC} . Both have been normalised by the diagonal elements of $\text{Cov}_{X/Y}$, therefore the diagonal is 1 by construction on the left panel, and the fact that it is very close to 1 on the middle panel proves the agreement between the two estimates. Off-diagonal elements are polluted on Cov_{MC} by numerical noise (which is one order of magnitude smaller than the diagonal elements and would reduce with more simulations). On the right panel, the absolute difference between the two estimates of the covariance matrix (non-normalised) is shown, element-wise divided by the standard deviation of Cov_{MC} (obtained from bootstrapping the simulated pseudo spectra). Note the different colour scale of the right panel: the deviation is at most of order 1σ , showing good agreement between our two estimates and validating eq. (23).

where δ_p is the simulated overdensity at pixel p and \bar{N} is the mean number of galaxies per pixel (different for the three samples). A reconstructed density map is then built using eq. (17), which now incorporates Poisson shot-noise. These full-sky maps are then masked and their pseudo spectra are evaluated. The mean of the estimated pseudo spectra is compared with that of the theoretical pseudo spectra computed using the mixing matrices on Figure 6, proving strong agreement and validating the estimator.

The empirical covariance of the sets of pseudo spectra is finally computed and compared to the semi-analytical covariance we use throughout this analysis. The result in Figure 7 shows good agreement and validates the estimator and the simulation of the matrices \mathbf{X} and \mathbf{Y} (that were computed using generic spectra, see Appendix A).

The statistical pipeline is validated by performing a Monte Carlo analysis similar to the one performed in Penna-Lima et al. (2014). Specifically, we want to check if the estimated parameters are unbiased. For that purpose, given the adopted fiducial model, we use the likelihood as the probability distribution of the pseudo spectra \tilde{C}_ℓ^{AB} to generate random samples (*i.e.* sets of stacked vectors \tilde{C}^{obs}). For each sample, we fit all parameters to be tested, thus building a collection $\{\theta_i\}$ of best-fit values for these parameters. At step n , the means $\bar{\theta}_n = \sum_{i=1}^n \theta_i / n$ and standard deviations of the collection of best-fit values are computed. The largest relative error (LRE) over parameter means is computed and we repeat the process, adding more samples, until the LRE has reached a level of 0.1% and check that the fiducial values are within the error bars. For this test, we only use one sample of galaxies with the redshift distribution of the CMASS sample and generate samples of $\tilde{C}_\ell^{\kappa_{\text{CMB}} \times \kappa_{\text{CMB}}}$, $\tilde{C}_\ell^{\kappa_{\text{CMB}} \times \delta_{\text{CMASS}}}$ and $\tilde{C}_\ell^{\delta_{\text{CMASS}} \times \delta_{\text{CMASS}}}$. Results of this test are plotted in Figures 8 and 9, showing respectively the evolution of the mean values of the best fit parameters $\bar{\theta}_n$ as a function of the number of realisations n and the distribution of the best-fit parameters for those same realisations.

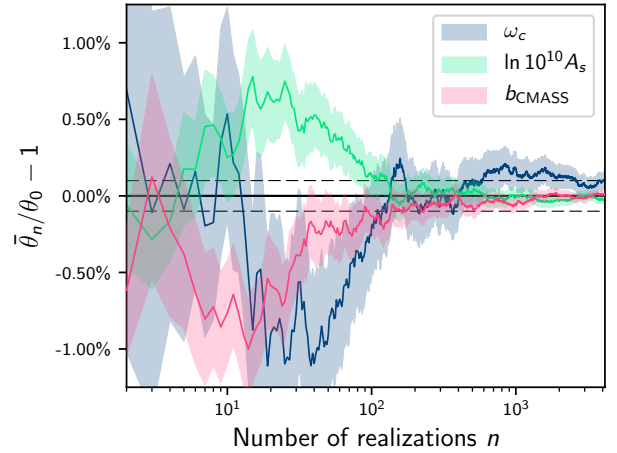


Figure 8. Statistical pipeline validation with Monte-Carlo simulation: realisations of the pseudo spectra are drawn from the likelihood \mathcal{L} and best-fit parameters $\theta = (\omega_c, \ln 10^{10} A_s, b_{\text{CMASS}})$ are computed. The relative error on the mean values of best-fit parameters $\bar{\theta}_n$ as a function of the number of realisations n is shown here. The dotted lines show the 0.1% requirement for this test, reached after 4146 realisations. The variance (displayed by the coloured bands) decreases as $1/\sqrt{n}$ while the mean values converge towards their input values, demonstrating the internal consistency of the statistical pipeline. Note however the very small deviation on ω_c , within the error requirement, but in accordance with the fact that the maximum likelihood estimator is consistent only asymptotically unbiased.

They confirm that the parameters' estimators are unbiased at least at the 0.1% level.

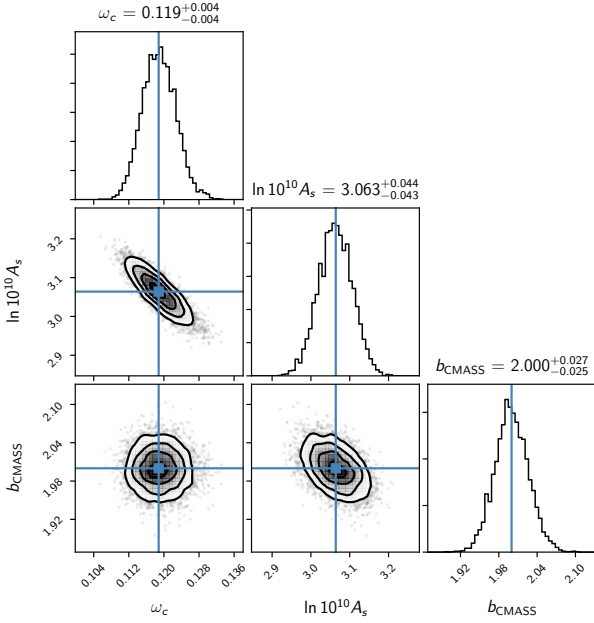


Figure 9. Same test as Figure 8, now showing the distribution of best-fit parameters for 4146 realisations. The ellipses show the 0.5, 1, 1.5 and 2σ contours and the blue lines show the input values of the parameters.

4.3 Null tests

We present in this section null tests that were performed to exclude potential systematic errors related to the masks and selection of the spectroscopic tracers.

In order to assess potential leakage of power in the cross spectra due to the masking, we cross-correlate the 100 simulated reconstructed lensing maps of the Planck Legacy Archive with the observed density maps of the three galaxy samples, and then correlate the observed lensing map with 100 simulated galaxy maps. This procedure removes cosmological angular correlation, and what correlation remains will be linked to the masks themselves. We find that all results are consistent with no correlation, excluding strong contamination from masking. We also measure the cross spectra between the galaxy and quasars sample and find marginal correlations, well below the auto-correlation signals.

Variable observational conditions during the SDSS photometric survey could potentially result in non-uniform selection functions of the galaxy and quasar samples, and introduce artificial power in the auto spectra at large scales. In order to exclude dramatic power leakage, we constructed maps of resolution $N_{\text{side}} = 64$ of the seeing, sky flux (for the g , r and i bands) and air mass of the photometric observations that were used to select galaxies and quasars in the spectroscopic catalogs,¹³ and we verify that the cross power spectra with the density maps (built in Section 3.2.3) are consistent with a null value. To do so, we approximate the

¹³ To do so, we made use of the CasJob service of the SDSS SkyServer, at <http://skyserver.sdss.org/casjobs/>.

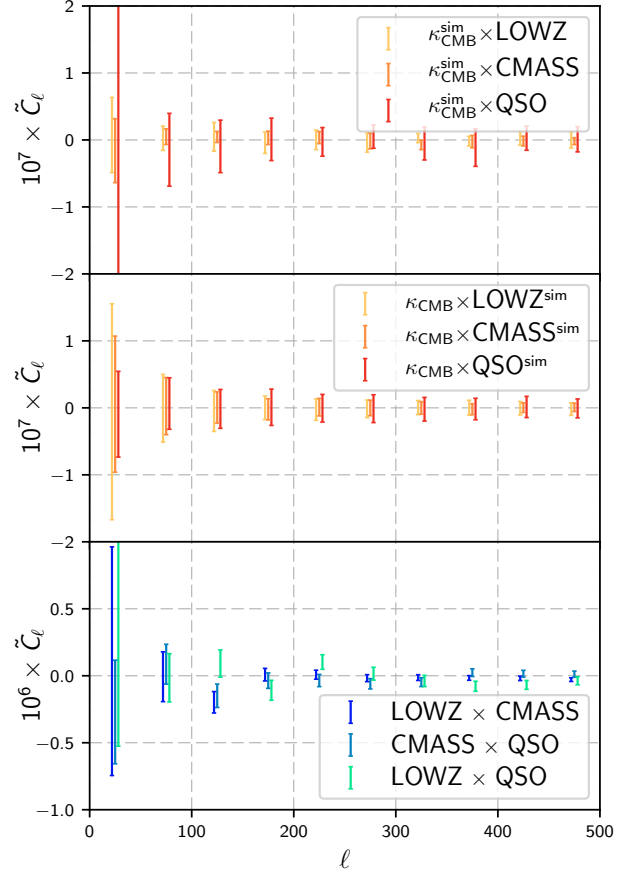


Figure 10. Null test for residual correlation. The top panel shows the mean cross-pseudo spectrum between simulated lensing maps and the real galaxy/quasar density maps, the middle panel shows the mean cross-pseudo spectrum between the real lensing map and simulated galaxy/quasar density maps, and the bottom panel shows the cross-pseudo spectra between the tracers. The cross-correlations with simulated maps are consistent with zero, showing no leakage of power from the masks, while the cross-correlation of the tracers show marginal correlation, at worst one order of magnitude lower than the autocorrelation signals.

error bars on the cross spectra by

$$\Delta^2 \left(\tilde{C}_\ell^{\text{syst} \times \delta_g} \right) \approx \frac{\hat{C}_\ell^{\text{syst}} \hat{C}_\ell^{\delta_g}}{2\ell + 1}, \quad (28)$$

where $\hat{C}_\ell^{\text{syst}}$ and $\hat{C}_\ell^{\delta_g}$ are the measured pseudo auto spectra of the systematics and density maps, respectively. Figures 11, 12 and 13 show the measured cross power spectra $\tilde{C}_\ell^{\text{syst} \times \delta_g}$ for multipoles $0 \leq \ell \leq 100$: they are consistent with no correlation, with no discernable trend across multipoles. Assuming that our approximation of the error is correct, we construct a χ^2 statistics as the sum of squared errors,

$$\chi^2 = \sum_{\ell=0}^{100} \left(\frac{C_\ell^{\text{syst} \times \delta_g}}{\Delta C_\ell^{\text{syst} \times \delta_g}} \right)^2, \quad (29)$$

and find generally acceptable agreement with a null correla-

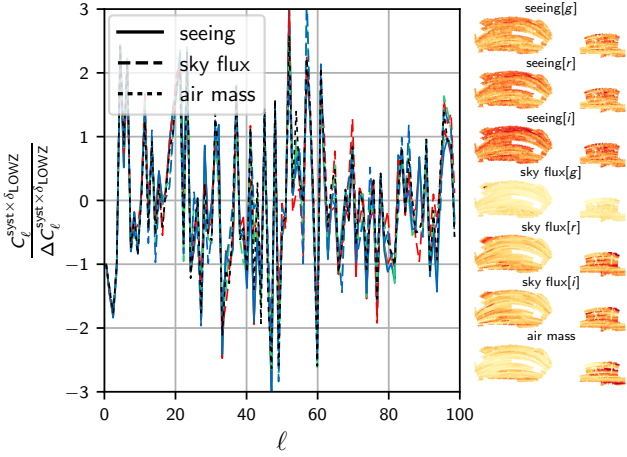


Figure 11. Null test of photometric systematics contamination: normalised large-scale cross spectra of the seeing (solid lines), sky flux (dashed lines) and air mass (dotted line) during photometric observations with the density of LOWZ galaxies. They are consistent with zero, with no discernable trend across multipoles. The seeing and sky flux are shown in the three main colour bands (g , r and i) which are displayed in red, green and blue. The maps of these observables are shown on the right in equatorial coordinates where the north and south galactic caps of the SDSS survey can be seen. The χ^2 statistics for these cross spectra are respectively 127, 132, 130, 121, 127, 127 and 133 for the seven observables listed on the right, for 101 degrees of freedom, excluding a large contamination.

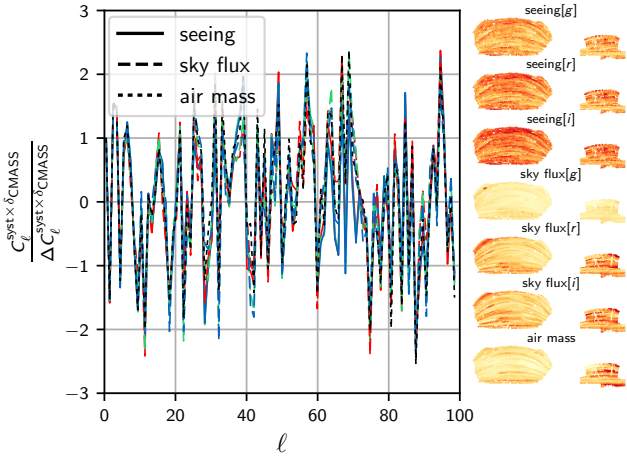


Figure 12. Same as Figure 11 for the CMASS galaxies. The χ^2 statistics are respectively 109, 111, 107, 114, 118, 108 and 123.

tion (with a rejection significance at worst 2.4σ for LOWZ with the seeing or airmass). However, this test can be misleading if we over- or underestimate the error. We partially relax the hypothesis on the error and suppose there is an unknown scale factor with respect to the true one. Considering the normalised spectra $x_\ell = C_\ell^{\text{syst} \times \delta_g} / \Delta C_\ell^{\text{syst} \times \delta_g}$ as independent, identically distributed random variables with the same mean and unknowns variance, we perform one-sample t -tests that reveal no significant departure from a null mean

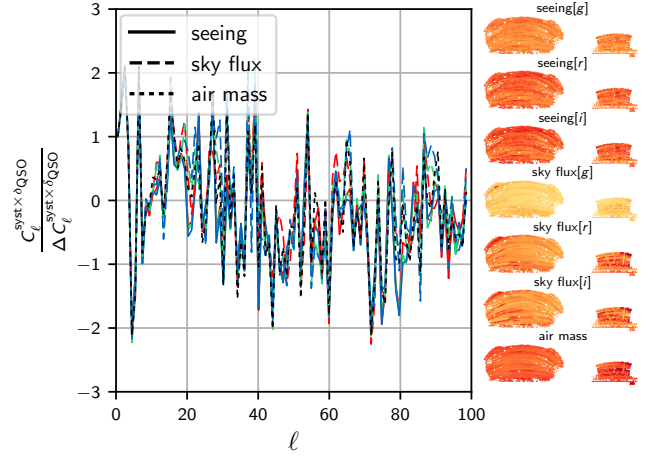


Figure 13. Same as Figure 11 for the quasar sample. The χ^2 statistics are respectively 82, 80, 81, 78, 86, 91 and 85.

over the multipole range, with p -values always greater than 0.5. From these tests, we conclude that photometric systematics do not strongly correlate with the overdensity maps.

5 ANALYSES AND RESULTS

5.1 Cosmological model

Our base model is the standard Λ CDM model with flat spatial sections (hence $\Omega_k = 0$) and a DE component with equation of state $w = -1$. The base parameters are the present-day baryon and CDM densities, $\omega_b \equiv \Omega_b h^2$ and $\omega_c \equiv \Omega_c h^2$, respectively – where $\Omega_i = \rho_i / \rho_c$ is the ratio of the component's energy density to the critical energy density ρ_c –, the Hubble constant today $H_0 = 100 h \text{ km/s/Mpc}$, the redshift of reionization z_{re} , the logarithm of the primordial curvature ζ dimensionless power spectrum $\ln 10^{10} A_s$ and its tilt n_s such that

$$\mathcal{P}_\zeta(k) = A_s \left(\frac{k}{k_0} \right)^{n_s - 1}, \quad (30)$$

with the pivot scale $k_0 = 0.05 \text{ Mpc}^{-1}$. We include massive neutrinos, parametrised by the effective number of neutrinos in the relativistic limit $N_{\text{eff}} = 3.046$ (taking into account non-instantaneous decoupling), an effective temperature $T_\nu/T_\gamma = 0.71611$, where T_γ is the photon temperature (slightly departing from $(4/11)^{1/3}$ to take into account neutrino heating from electron/positron annihilation, see Lesgourgues et al. 2009), and using one massive neutrino of mass $m_\nu = 0.06 \text{ eV}$ and two massless neutrinos, consistent with the Planck base Λ CDM model. The linear matter power spectrum $P_m(k, z)$ and the CMB temperature power spectrum C_ℓ^{TT} are computed using the Cosmic Linear Anisotropy Solving System (CLASS) as a backend to NumCosmo. The non-linear matter power spectrum is computed using a Halofit prescription (Smith et al. 2003b) implemented in NumCosmo, with parameters from Takahashi et al. (2012b), modified to take into account neutrinos as in CLASS. Reionization is modelled in a CAMB-like fashion (Lewis et al. 2000) and parametrised by the mid-point z_{re} ,

fixed width $\Delta z_{\text{re}} = 0.5$, and includes Helium reionization at a fixed redshift $z_{\text{re}}^{\text{He}} = 3.5$. Recombination is computed within CLASS and Big Bang nucleosynthesis is computed with PArthENoPE¹⁴ (Pisanti et al. 2008).

From the constraints that we will obtain in our analyses, we will also estimate the total matter density parameter¹⁵ $\Omega_m = \Omega_b + \Omega_c + \Omega_\nu$, the optical depth to the last scattering surface τ and the variance of the linear matter density fluctuations σ_8^2 in spheres of radius $R = 8 h^{-1}$ Mpc extrapolated to $z = 0$,

$$\sigma_8^2 = \int dk \frac{k^2}{2\pi^2} P_m(k, z=0) |W(k, R)|^2, \quad (31)$$

where the top-hat window function is $W(k, R) = 3j_1(kR)/kR$ and the matter power spectrum is computed from linear theory.

5.2 Statistical analysis

In this section, we describe our Bayesian statistical analysis and present constraints on cosmological parameters of the Λ CDM model and the galaxy/quasar biases.

We first apply the Markov Chain Monte Carlo (MCMC) approach using only CMB lensing-LSS correlations data – the set of the six auto and cross spectra of CMB lensing and BOSS galaxy and quasar overdensities, as shown in Figure 4 – and varying only a subset of cosmological parameters in order to assess the constraining power of these. In particular, we also consider different combinations of the auto and cross spectra to measure the effects on the parameter constraints provided by these probes. Then, we add CMB temperature information and obtain constraints on the Λ CDM model and extensions including the mass of neutrinos – that impacts small-scale structure formation – and the DE equation of state w – that impacts the expansion in the low redshift Universe.

We run the MCMC algorithm using an *ensemble sampler*¹⁶ with many walkers (100 to 1000), moving their positions in the parameter space as an ensemble *via a stretch move* scheme (Goodman & Weare 2010) implemented in NumCosmo. We monitored the convergence of the chains using three numerical tools, namely the Multivariate Potential Scale Reduction Factor (MPSRF, Gelman & Rubin 1992; Brooks & Gelman 1998), the Heidelberger-Welch test (Heidelberger & Welch 1981, 1983) and the Effective Sample Size (ESS); see Appendix D for more details.

These diagnostics can fail in different situations. For this reason, we also performed three different visual inspections for each parameter:

- (i) the parameter trace plot, *i.e.* the value of the parameter for a given walker *vs* iteration time.
- (ii) the ensemble distribution trace plot, that is, the empirical ensemble distribution given by the walkers' positions *vs* iteration time. This allows us to monitor the evolution of the ensemble mean and variance.

- (iii) the total mean *vs* the cumulative sum of the ensemble means: if the chain has reached convergence, the difference (scaled by the spectral density at null frequency) is distributed as a brownian bridge, the L_2 norm of which is used in the Schruben test.

For all MCMCs, we ran them until all the relative errors of the means were smaller than 10^{-2} ; at this point, we applied all the tests above, and if the chains failed some of them, we continued the run until all tests were satisfied.

5.2.1 Constraints from CMB lensing-LSS correlations

Data from CMB lensing and spectroscopic tracers of matter alone cannot efficiently constrain all cosmological parameters. However, we want to highlight the cosmological information carried by these probes. To do so, we perform several MCMC analyses considering a subset of free cosmological parameters. These are only illustrative in the sense that the posterior distribution of cosmological parameters will be shrunk from fixing some others.

The theoretical spectra have different dependences on the cosmological parameters and galaxy/quasar biases. The most explicit dependencies of the angular spectra \bar{C}_ℓ are on the power spectrum amplitude (A_s or σ_8), the matter density parameter Ω_m and the galaxy/quasar biases (see the kernels in Section 2.1):

$$C_\ell^{\kappa\kappa} \propto \Omega_m^2 A_s \quad (32)$$

$$C_\ell^{\kappa\delta_g} \propto \Omega_m b_g A_s \quad (33)$$

$$C_\ell^{\delta_g\delta_g} \propto b_g^2 A_s. \quad (34)$$

This system is closed, *i.e.* in principle, comparing the various auto and cross spectra should allow for a non-degenerate estimation of the parameters.

Therefore, we run MCMCs freeing ω_c , $\ln 10^{10} A_s$ and the galaxy/quasar biases, and fixing all other cosmological parameters. Their fiducial values are from Planck 2015 “TT,TE,EE+lowP+lensing+ext” best fits (Planck Collaboration et al. 2016f). We assume flat prior distributions over wide ranges (larger than the sampled ranges). In order to distinguish and quantify the information contained in the various measured auto and cross spectra, we try different combinations. That is, we run an MCMC with the full dataset (“ $\kappa\kappa+\kappa\delta_g+\delta_g\delta_g$ ”), and then repeat without the cross spectra (“ $\kappa\kappa+\delta_g\delta_g$ ”), without the CMB lensing auto spectrum (“ $\kappa\delta_g+\delta_g\delta_g$ ”) and without the galaxy auto spectra (“ $\kappa\kappa+\kappa\delta_g$ ”). We run these chains with 100 walkers to ensure a good mixing. Their MPSRFs are below 1.02 and the correlation lengths are of order 20-40, varying amongst parameters.

The sampled posterior distributions of these parameters are shown in Figure 14 for the full dataset and the three subsets aforementioned. We note that the “ $\kappa\delta_g+\delta_g\delta_g$ ” and “ $\kappa\kappa+\kappa\delta_g$ ” subsets, dominated by respectively galaxy clustering and CMB lensing information, provide complementary information, since the correlations between the parameters, except those in the (b_{LOWZ} , b_{CMSS}) plane, present different alignments (see the orange and yellow confidence regions in Figure 14). Therefore, the constraints on the parameters are greatly improved when combining both auto spectra, “ $\kappa\kappa+\delta_g\delta_g$ ”. Apart from the constraints on b_{LOWZ} , b_{CMSS} ,

¹⁴ <http://parthenope.na.infn.it/>

¹⁵ The DE density parameter today is $\Omega_\Lambda \approx 1 - \Omega_m$ since we consider only flat space sections (neglecting radiation).

¹⁶ Some authors refers to ensemble samplers as *population Monte Carlo*.

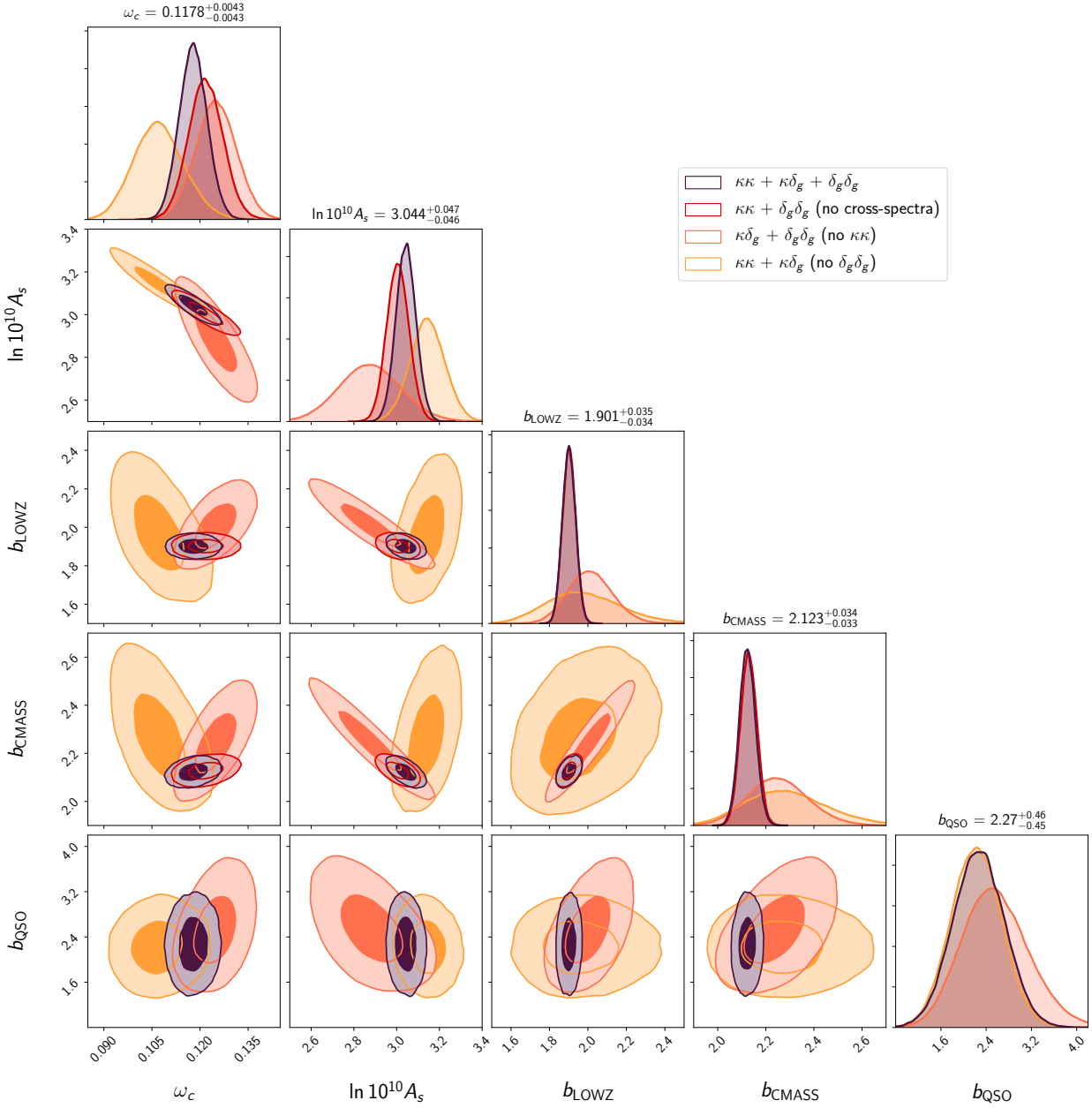


Figure 14. One and two-dimensional projections of the posterior distribution sampled by the MCMC algorithm for the CMB lensing-LSS correlations. Biases, ω_c and A_s are sampled, the other cosmological parameters being fixed at Planck 2015 “TT,TE,EE+lowP+lensing+ext” best fit values. The contours show the 1- and 2- σ confidence regions for subsets of our data. The values of the parameters above the histograms are the medians with asymmetrical errors (the 16th and 84th percentiles corresponding to $\pm\sigma$ for a Gaussian distribution). The $(\ln 10^{10} A_s, \omega_c)$ plane illustrates the degeneracy breaking and the confidence region shrinkage due to the addition of the cross spectra (compare the dark purple and burgundy contours). The integral of the histograms are normalised to unity, therefore in the approximation of Gaussian distributions, the maxima of the histograms are inversely proportional to the standard deviation of the parameters, allowing to directly read the improvement of the constraints. Note that the quasar bias is not fitted for the subset including only auto spectra (“ $\kappa\kappa + \delta_g\delta_g$ ”).

which are already strongly determined by galaxy density auto spectra, the additional information contained in the cross spectra narrows the distribution, as can be observed in the $(\ln 10^{10} A_s, \omega_c)$ plane by comparing the confidence regions for “ $\kappa\kappa + \delta_g\delta_g$ ” (in burgundy) with “ $\kappa\kappa + \kappa\delta_g + \delta_g\delta_g$ ” (in dark purple). The addition of the cross spectra decreases the statistical error by 10% for $\ln 10^{10} A_s$ and 20% for ω_c , and

slightly shifts the best fits (by less than 1 σ). This plane is translated into the (σ_8, Ω_m) plane in Figure 15 where the degeneracy breaking expected from the joint analysis is highlighted.

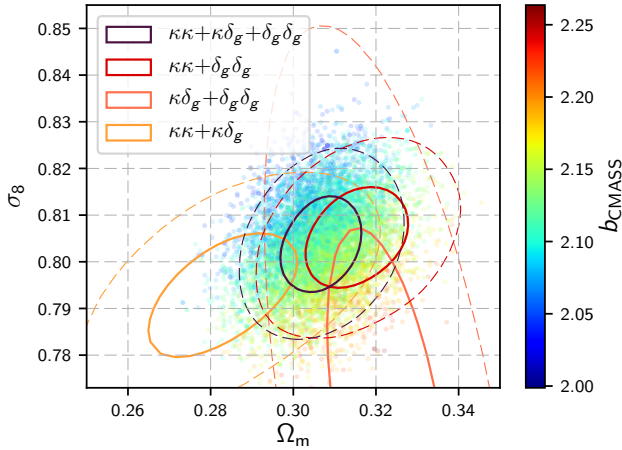


Figure 15. Confidence regions for σ_8 and Ω_m corresponding to the distributions sampled by the ensemble sampler MCMC algorithm for the CMB lensing-LSS correlations dataset only, with the other cosmological parameters fixed at Planck 2015 “TT,TE,EE+lowP+lensing+ext”, and various subsets of the dataset. 1σ contours (respectively 2σ contours) are represented by solid (dashed) lines. CMB lensing and galaxy densities show different degeneracies, that are partially broken by combining the observations. Coloured points are samples from the full dataset chains, that show how σ_8 , Ω_m and galaxy biases are degenerated.

5.2.2 Constraints on Λ CDM from CMB temperature and CMB lensing-LSS correlations

In this section, we carry out the analysis combining CMB temperature and the correlations of CMB lensing and galaxy/quasar densities used in the previous section (that is all six power spectra of Figure 4) to obtain constraints on the cosmological parameters of the Λ CDM model (ω_b , ω_c , H_0 , z_{re} , $\ln 10^{10} A_s$ and n_s). The results of this analysis will be denoted “CMB TT + CMB lensing \otimes LSS” in the figures. In addition, we run, for comparison, the MCMC algorithm using only CMB temperature data (“CMB TT ”), and CMB temperature and lensing (“CMB TT + CMB lensing”). We neglect the correlation between CMB temperature and the matter density at later times (either baryonic matter in galaxies and quasars or dark matter weighted by CMB lensing), *i.e.*, we neglect the late ISW effect, as it is not yet detected with a strong significance (Planck Collaboration et al. 2016h; Nicola et al. 2016), and we discuss possible consequences in Section 5.3. In practice, this means that we approximate the total likelihood by the product of the CMB temperature and CMB lensing-LSS correlations likelihood functions.

We use the Planck likelihood codes `Plik` and `Commander` (Planck Collaboration et al. 2016d) respectively for high and low multipoles of the temperature-only power spectrum C_ℓ^{TT} . The likelihood code introduces 15 additional nuisance parameters related to foreground and instrument models (A_{217}^{CIB} , $\xi^{\text{tSZ} \times \text{CIB}}$, A_{100}^{tSZ} , A_{143}^{PS} , $A_{143 \times 217}^{\text{PS}}$, A_{217}^{PS} , A^{kSZ} , A_{100}^{dustTT} , A_{143}^{dustTT} , $A_{143 \times 217}^{\text{dustTT}}$, A_{217}^{dustTT} , c_{100} , c_{217} and y_{cal} ; see Planck Collaboration et al. 2016d). We use the profile likelihood to speed up our MCMC analyses, subfitting the nuisance parameters for each set of cosmological parameters.

We describe this methodology in Appendix B, and also show that it does not affect the results on cosmological parameters.

Figure 16 shows the constraints on the base Λ CDM model’s parameters for the three aforementioned data combinations. When using CMB TT only, we find parameter constraints that are in perfect agreement with the Planck analysis.¹⁷ The strong degeneracy observed between the power spectrum amplitude A_s and the reionization redshift z_{re} corresponds to the amplitude of the power spectrum of CMB temperature anisotropies, which is proportional to $A_s e^{-2\tau}$ where τ is the optical depth to the last scattering surface, strongly dependent on reionization history. Adding CMB lensing drives A_s and z_{re} towards lower values with a shift of about 1σ for each parameter as evinced by the one- and two-dimensional projection of the posterior distributions. Finally, adding information of LSS tracers (both the auto-correlations and cross-correlations with CMB lensing) provides slightly smaller contours and, therefore, they do not significantly help in breaking this degeneracy. We find no significant improvement for τ or σ_8 , although it is consistent with the constraints from CMB lensing. In the (σ_8, Ω_m) plane (see Figure 17), we observe that early Universe data favors bigger values of σ_8 than the late one, as reported repeatedly (Hildebrandt et al. 2016; Planck Collaboration et al. 2016j). Whether this is indication of new physics or a systematics artefact is beyond the scope of this work, but it might be an important issue in the future.

Nonetheless, there is an improvement of order 20% on the measurements of H_0 and ω_c . We find $H_0 = 68.7 \pm 0.9$ km/s/Mpc, slightly higher than CMB temperature alone – albeit still lower than distance measurements from supernovae (Riess et al. 2016) or time delays in strong lensing (Bonvin et al. 2017) – and $\omega_c = 0.117 \pm 0.002$ as the degeneracy between A_s and ω_c is broken by the lensing-LSS correlations (see Figure 14). This results in a constraint on the matter density parameter $\Omega_m = 0.296 \pm 0.011$. Additionally, we obtain strong constraints on the biases of the galaxy samples, respectively

$$\begin{aligned} b_{\text{LOWZ}} &= 1.855 \pm 0.037 \\ b_{\text{CMSS}} &= 2.077 \pm 0.036. \end{aligned} \quad (35)$$

These 4% constraints are in general agreement with previous measurements (Ho et al. 2012). Our analysis has the advantage that our data is model-independent in the sense that estimating pseudo spectra \tilde{C}_ℓ does not require any assumption on cosmology since we don’t measure distances. Moreover, all the cosmological parameters of the Λ CDM model are fitted jointly. Note, however, that our modelling assumes a constant bias, that can be interpreted as a redshift- and scale-averaged bias, when other analyses used a scale-dependent bias (in the form of a Taylor expansion, *e.g.* in Gil-Marín et al. (2016)) or simply more redshift bins. Interestingly, the analysis also shows significant correlations between the biases and cosmological parameters, in particular with ω_c , H_0

¹⁷

The detailed results of the Planck MCMC analyses are available here: https://wiki.cosmos.esa.int/planckpla2015/images/f/f7/Baseline_params_table_2015_limit68.pdf

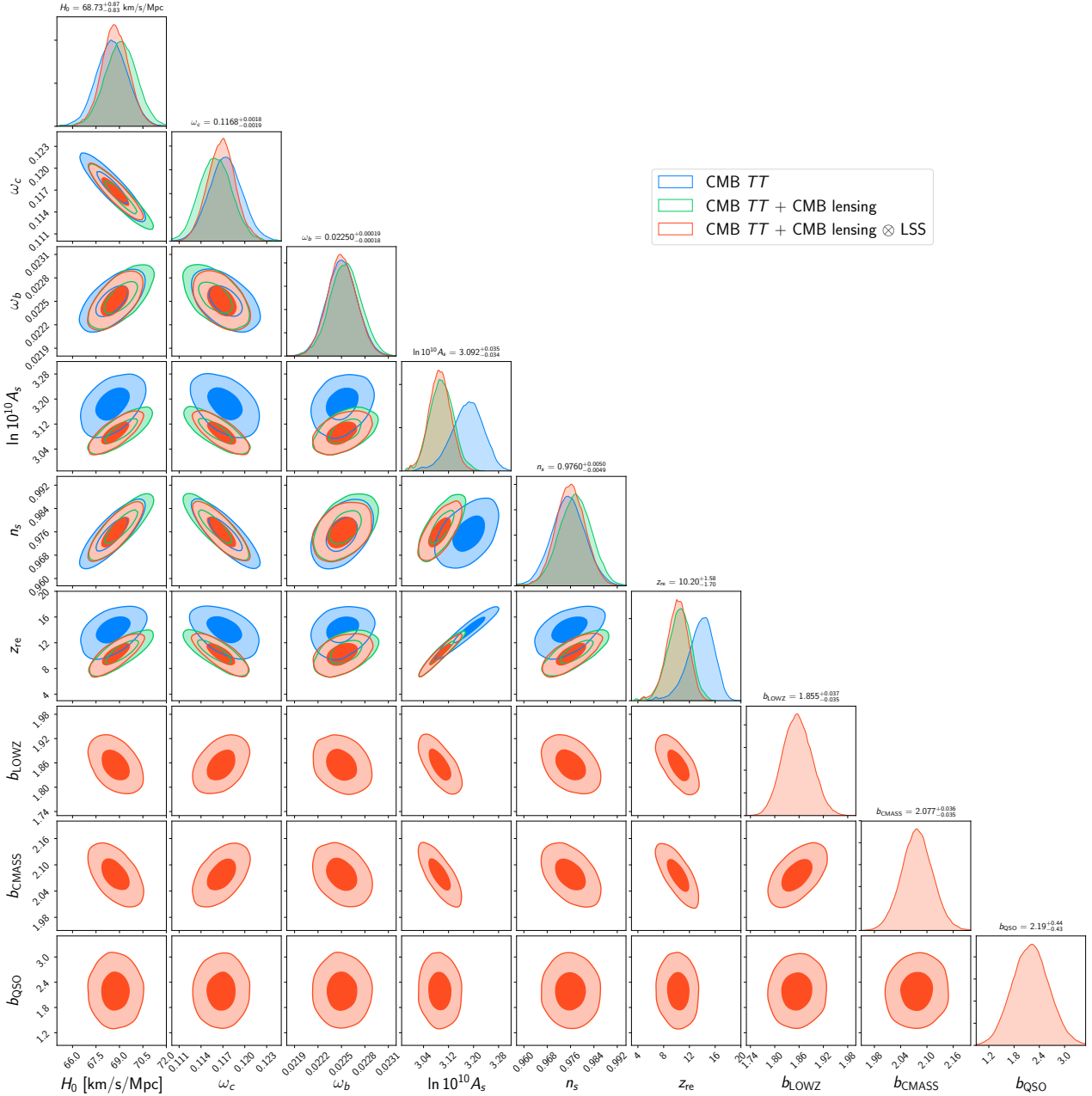


Figure 16. Constraints on the parameters of the base 6-parameters Λ CDM model and galaxy biases. Confidence regions are shown respectively in blue, green and red for CMB temperature only, CMB temperature combined with CMB lensing, and the joint analysis of CMB temperature and the correlations of CMB lensing and LSS tracers. The constraints above the marginal posteriors are for this last data set.

and A_s . If one considers biases as effective parameters encoding structure formation and clustering of galaxies, these correlations can shed light on the astrophysical and cosmological processes governing the formation of such structures. Finally, we also obtain a broad constraint on the bias of the uniform sample of quasars from the cross-correlation with CMB lensing

$$b_{\text{QSO}} = 2.19 \pm 0.44. \quad (36)$$

This value is in tension with other measurements (White et al. 2012; DiPompeo et al. 2015; Laurent et al. 2016, 2017) that found a bias of order 3 to 4 (although they did as-

sume a cosmology). We found no difference when fitting for this bias when using data from only the northern or southern galactic caps, excluding a possible strong asymmetry and contamination of higher multipoles. We note a surprising trough in the $\tilde{C}_{\ell}^{\text{CMB} \times \text{QSO}}$ cross spectrum (see Figure 4) around $\ell \sim 400$ that we could not explain. However, this bias directly depends on the amplitude of lensing that may be underestimated (Planck Collaboration et al. 2014).

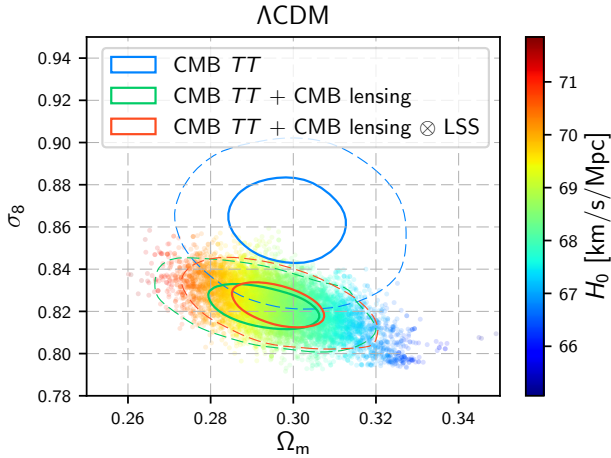


Figure 17. Constraints on σ_8 and Ω_m for the 6-parameter base Λ CDM model from the combination of CMB temperature and the correlations of CMB lensing and spectroscopic tracers. The 1 and 2 σ contours are represented by the respectively solid and dashed lines. The coloured points show the degeneracy with H_0 (in km/s/Mpc) and are samples from the “CMB TT + CMB lensing \otimes LSS” chain.

5.2.3 Constraints on the mass of neutrinos m_ν and the dark energy equation of state w

In the next set of MCMCs, we additionally sample the mass of neutrinos m_ν (with one massive and two massless neutrinos) or the DE equation of state w (where w is constant over time) separately and compare the performance of the joint analysis in these extended models.

In the first case, we find that the joint analysis yields a constraint on the neutrino mass of $m_\nu < 0.29$ eV [68%], dividing the higher bound by a factor of two with respect to the constraint from CMB TT alone (see Figure 18). A non-zero mass is not detected with strong statistical significance, but the best fit we obtain around $m \sim 0.12$ eV is in agreement with lower bounds around 0.05 eV derived from neutrino oscillations (Olive 2014) and cosmological upper bounds, *e.g.* that derived from the combination of CMB and the Lyman- α forest power spectrum of 0.12 eV from Palanque-Delabrouille et al. (2015). As shown in Figure 19, the galaxy auto power spectra are sensitive to the mass of neutrinos as they can probe small scales at low redshift, where massive neutrinos tend to smooth out density fluctuations. This means that the mass of neutrinos should be positively correlated with galaxy biases, which is indeed observed in the lower panels of Figure 18. We also observe that adding LSS information significantly improves the constraints on the other cosmological parameters in this extended model. Because of the anti-correlation between H_0 and the mass of neutrinos, the joint analysis favours a higher expansion rate $H_0 = 67.76^{+1.20}_{-1.51}$ than CMB data alone. It also noticeably shifts the posterior distributions for z_{re} and A_s towards lower values, resulting in a lower value of the reionization optical depth $\tau = 0.090 \pm 0.020$.

In the second case, we release w , the mass of neutrinos being fixed to $m_\nu = 0.06$ eV. CMB temperature anisotropies are only very weakly sensitive to DE and CMB lensing

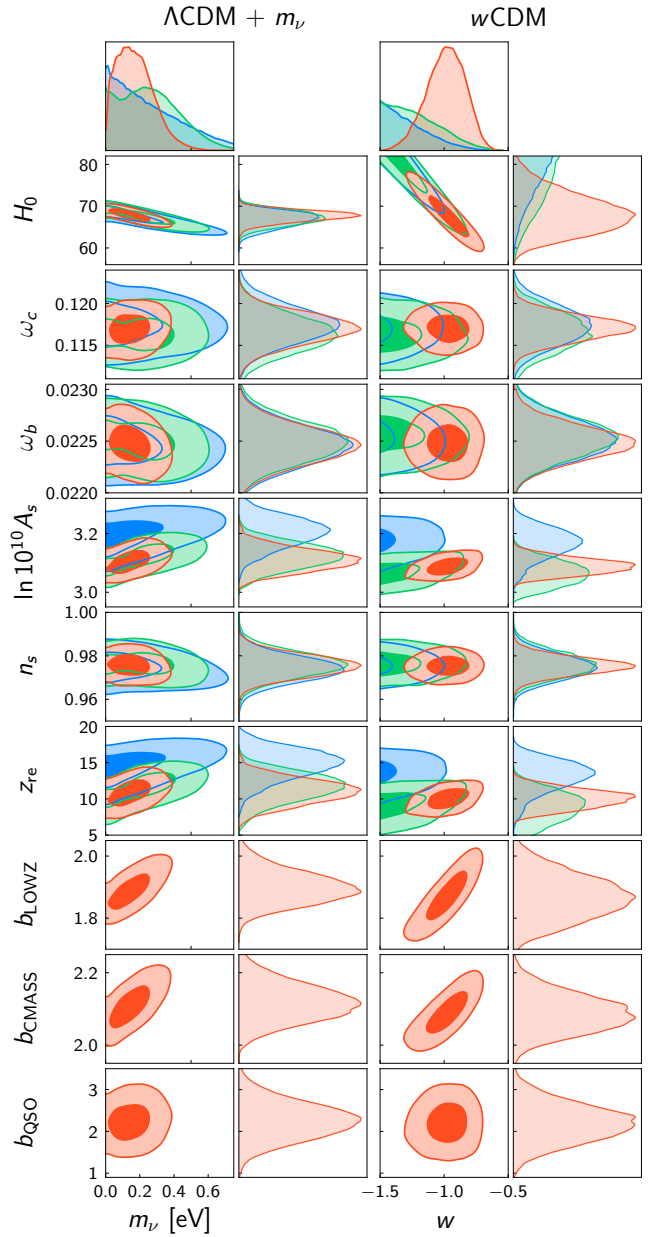


Figure 18. Cosmological constraints on two one-parameter extensions of the base 6-parameters Λ CDM model used here. On the column labeled Λ CDM + m_ν , the mass of the neutrinos m_ν (expressed in eV) is set free and sampled in addition to the six cosmological parameters and the galaxy and quasar biases, w being fixed to -1 . On the column labelled w CDM, w is set free and the mass of neutrinos is fixed at its fiducial value of 0.06 eV. Only the two-dimensional distributions involving m_ν or w are shown, together with marginal posteriors for the other cosmological parameters (rotated to match the leftmost vertical axes). The two upmost plots show the marginal distributions obtained for m_ν and w . The colours are the same as in Figure 16: blue is for CMB temperature alone, green is for CMB temperature and lensing and red is for CMB temperature and the CMB lensing-LSS correlations.

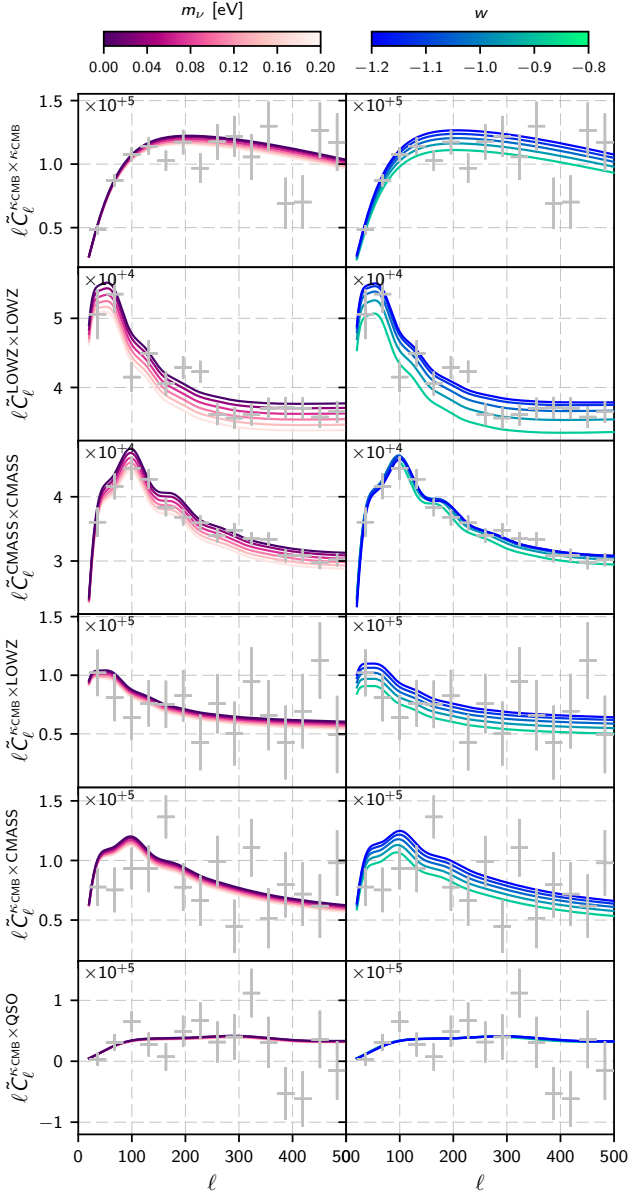


Figure 19. Theoretical pseudo spectra for different values of the mass of neutrinos m_ν and w . On the left column, m_ν varies from 0 eV (dark purple) to 0.20 eV (light pink); on the right column, w varies from -1.2 (green) to -0.8 (blue). Data points from Figure 4 are overlaid in light grey.

probes the Universe at redshift $z \sim 2$, where matter is still dominating; therefore these probes do not contain much information on w . Adding the correlations with LSS information becomes necessary and rewarding as it breaks the degeneracies of the constraints on H_0 , $\ln 10^{10} A_s$, z_{re} and w . We observe a strong anti-correlation between w and the Hubble parameter H_0 , meaning that observations can be matched by a more slowly expanding Universe with a more negative DE pressure. Constraints from the joint analysis ($w = -0.98^{+0.14}_{-0.16}$) are consistent with a cosmological constant ($w = -1$), while constraints from CMB favour a lower value of w . We also note a strong correlation between the

Table 1. Constraints on σ_8 , τ and Ω_m from the joint analysis of CMB temperature and CMB lensing–large-scale structure correlations.

Model	σ_8	τ	Ω_m
Λ CDM	$0.823^{+0.010}_{-0.010}$	$0.082^{+0.019}_{-0.019}$	$0.296^{+0.011}_{-0.011}$
Λ CDM + m_ν	$0.806^{+0.018}_{-0.023}$	$0.090^{+0.021}_{-0.020}$	$0.307^{+0.019}_{-0.015}$
w CDM	$0.816^{+0.044}_{-0.039}$	$0.080^{+0.015}_{-0.015}$	$0.303^{+0.044}_{-0.041}$
w CDM + m_ν	$0.786^{+0.045}_{-0.038}$	$0.097^{+0.024}_{-0.023}$	$0.328^{+0.046}_{-0.046}$

biases and w of 81% and 89% for CMASS and LOWZ respectively.

In summary, in both cases, constraints from the joint analysis are substantially better for almost all parameters because of its ability to break degeneracies related to the chosen new parameters. This result constitutes a forceful encouragement to perform this type of analysis when data from the next generation of surveys becomes available.

5.2.4 Constraints on w CDM + m_ν from CMB TT and CMB lensing–LSS correlations

Finally, in the last set of MCMC analyses, we release both the mass of neutrinos m_ν and the DE equation of state w and demonstrate that a joint analysis of currently available data can set constraints on a 8-parameter cosmological model (w CDM + m_ν). Similarly to the previous cases, the results are presented on Figure 20 for the full joint analysis and for CMB TT data, allowing for comparison. We find constraints that are in agreement with the current picture of the Λ CDM model as well as those obtained in the previous sections, with a value of $w = -0.93^{+0.14}_{-0.18}$ consistent with a cosmological constant. We obtain a higher bound on the mass of the neutrinos of $m_\nu < 0.29$ eV [68%] and a low value of the Hubble constant of $H_0 = 65.78^{+5.43}_{-4.35}$ km/s/Mpc, albeit with larger error bars. As opposed to the 6-parameter Λ CDM case, the joint analysis does not really outperform constraints from CMB TT data alone regarding the base parameters, except for H_0 which strongly correlates with w . In particular, the constraints on ω_c or n_s are not as strong. However, the additional information extracted by the joint analysis (partially) breaks the $w - H_0$ degeneracy, enabling for control of all eight cosmological parameters, plus the biases, *i.e.* eleven parameters in total. The correlation coefficient matrix reveals a strong correlation of galaxy biases with H_0 , w and m_ν (see Figure 21) indicating that upcoming surveys will require exquisite control of these biases to get tight constraints on w and its possible time evolution.

Because of the degeneracy between H_0 , w and m_ν , precision is lost on Ω_m , even though the physical density $\omega_m \equiv \Omega_m h^2$ is well constrained by CMB TT and CMB lensing even in this model (we find $\omega_m = 0.1413 \pm 0.0024$). In the (σ_8, Ω_m) plane (see Figure 22), we obtain constraints that are consistent from the joint analysis over the models tested here, with increasing degeneracy. We measure $\sigma_8 \Omega_m^{2.7} = 0.170 \pm 0.007$ from the joint analysis on the 8-parameter w CDM + m_ν model.

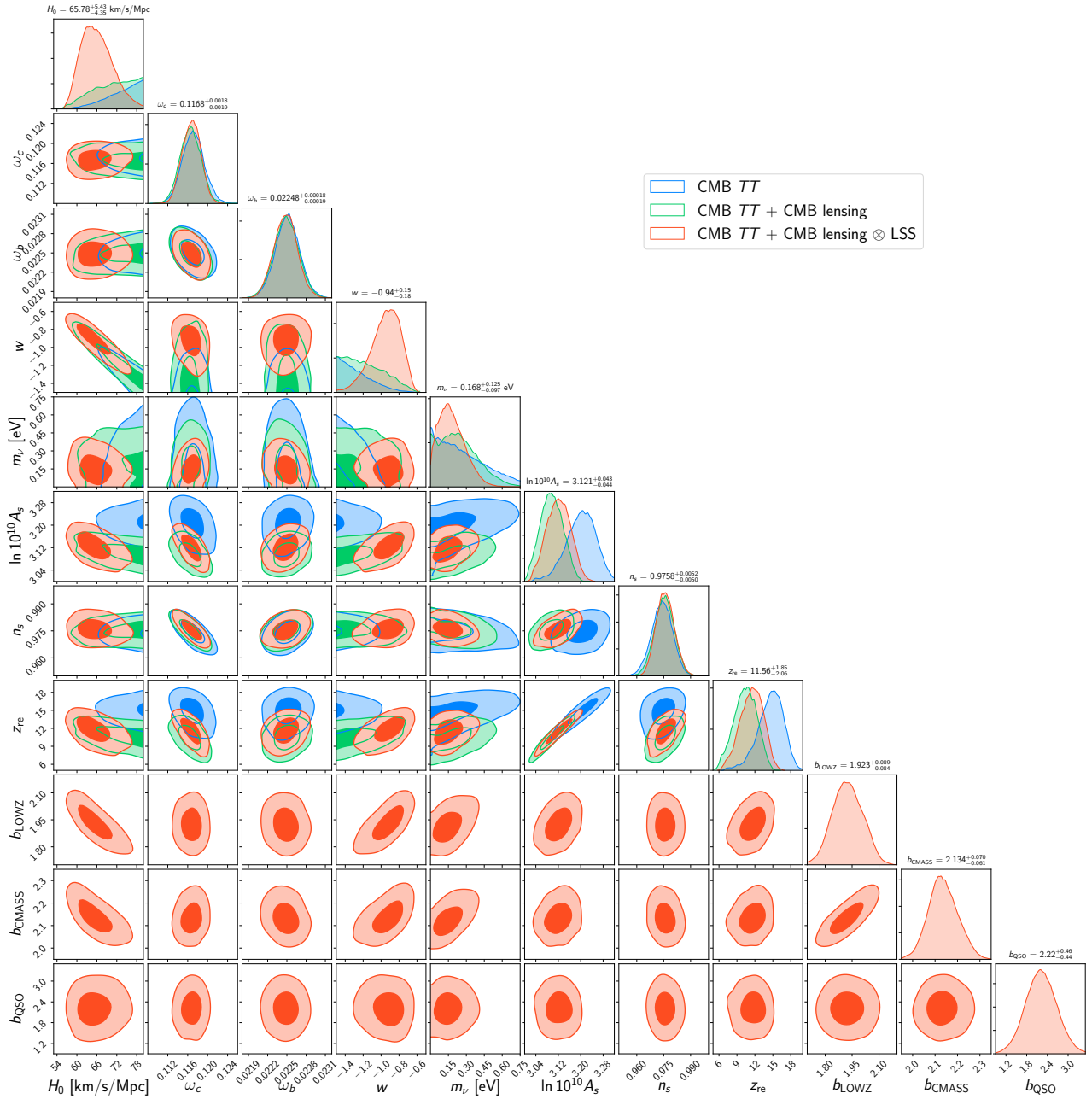


Figure 20. Constraints on the parameters of the w CDM + m_ν model and biases from the combination of CMB temperature and the correlations of CMB lensing and large-scale structure.

5.3 Limits and perspectives

Forecasts predict strong improvements of the constraints on cosmological parameters from the combination of the next generation galaxy surveys and CMB experiments (Pearson & Zahn 2014; Schaun et al. 2016a). One of the goals of this paper was to identify the difficulties in running joint analyses on real data, while acting as a proof of concept. We discuss in this section assumptions that were made and technical difficulties that we were able to pinpoint.

We neglected the correlation, generated by the ISW effect, between the CMB temperature map and the large-scale structure as traced by CMB lensing or spectroscopic tracers. This correlation originates in the net energy gain (loss) of

photons crossing gravitational potentials wells (hills) evolving thanks to dark energy. In principle, this would lead to underestimation of error bars on cosmological parameters. However, this correlation is weak and has not been detected with a strong statistical significance on SDSS galaxies: the signal-to-noise ratios for the correlation with the LOWZ and CMASS samples reported by the Planck collaboration is of order 2.4, and that with the lensing map (corresponding to a temperature bispectrum) is of order 3.2 (Planck Collaboration et al. 2016h). Therefore, taking this cross-correlation term into account would not dramatically change our constraints.

One possible source of systematics in the galaxy-lensing

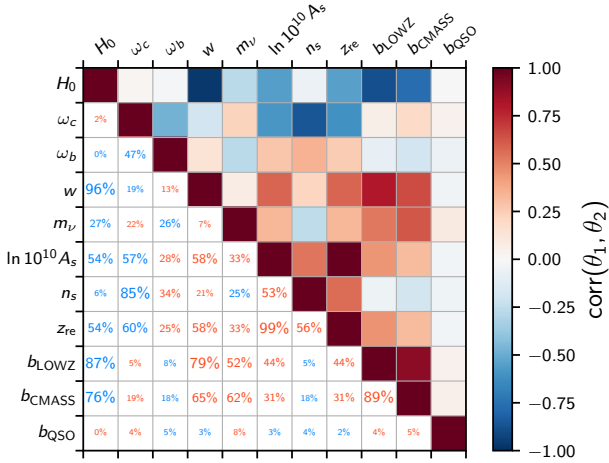


Figure 21. Correlation coefficient matrix of the w CDM + m_ν model's parameters and biases from the joint analysis of CMB temperature and the correlations of CMB lensing and large-scale structure (see the constraints on Figure 20). The upper triangle is colour encoded, red (respectively blue) meaning complete correlation (anti-correlation) between parameters. The lower triangle is given in percentage, written in red (blue) for positive (negative) correlation.

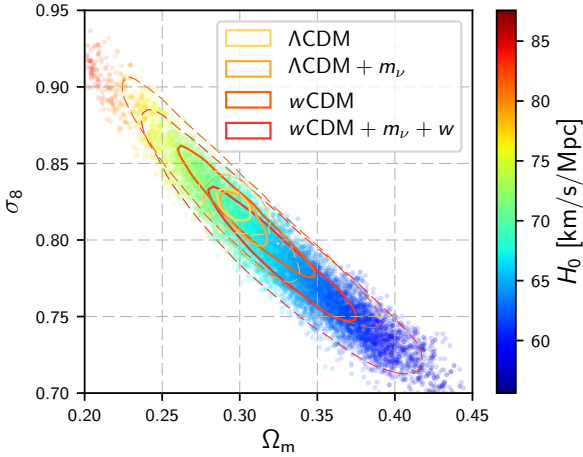


Figure 22. Confidence regions for σ_8 and Ω_m from the combination of CMB temperature and the CMB lensing-LSS correlations for the Λ CDM model and extensions to the mass of neutrinos m_ν and the dark energy equation of state w . The coloured points are samples from the w CDM + m_ν chain.

cross-correlations comes from the tSZ component separation that is required to produce the lensing map (Planck Collaboration et al. 2016b,c,i). Free electrons in hot galaxy clusters imprint a specific local spectral distortion on the CMB temperature map. These clusters must be identified and removed before measuring the spatial distortion due to gravitational lensing. If these clusters hold some of the galaxies in the samples we use, this might lead to a systematic underestimation of the lensing signal in the direction of these galaxies. Unfortunately, we were not able to access lensing maps using various reconstruction methods to test this hypothesis.

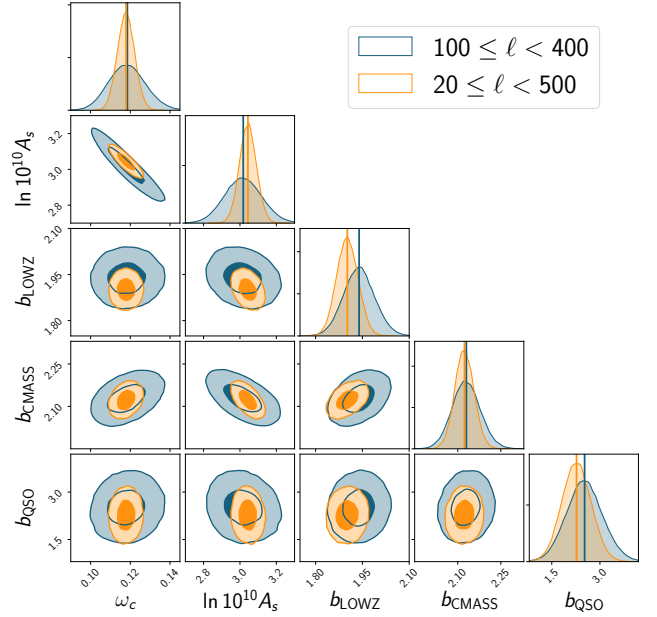


Figure 23. Comparison between the posterior distributions sampled by MCMC analysis using the CMB lensing-LSS correlations dataset for different multipole ranges: in orange, the constraints resulting from the full multipole range ($20 \leq \ell < 500$) used in the rest of this work, and in blue those resulting from a smaller multipole range excluding small and large scales ($100 \leq \ell < 400$). The distributions are compatible, which means that if there is a modelling issue either at large scales (e.g. due to the RSD) or at small scales (e.g. due to uncertainties in the non-linear matter power spectrum), it does not dramatically affect the constraints on cosmological parameters.

We now discuss theoretical uncertainties. The first one comes from the Limber approximation (LoVerde & Afshordi 2008): it fails at very large scales, the transition scale depending on the width of the redshift bin considered (Carpagne et al. 2017). In this work, we used very broad redshift bins and discarded low multipoles $\ell < 20$, so as to be in the safe regime of the approximation. We also did not consider redshift space distortion (RSD) for the same reasons (Alonso et al. 2015; Padmanabhan et al. 2007). To test that RSD or other large-scale effects were not driving parameter constraints inconsistently, we performed an MCMC analysis of CMB lensing-galaxy correlations on a smaller multipole range ($100 \leq \ell < 400$, see Figure 23) and found no significant deviation. However, future surveys aiming at measuring extremely large-scales (Alonso & Ferreira 2015) will require better modelling, especially for tomographic studies.

In this paper, we used a Gaussian likelihood and a Gaussian covariance, *i.e.* we did not incorporate higher order statistics of the matter density field nor the so-called super-sample variance due to the finite size of the surveyed volume and inaccessible modes therein (Schaan et al. 2014; Krause & Eifler 2016; Schaan et al. 2016a). At the current level of signal-to-noise ratio, these simplifications are safe but they should be lifted in future data analysis. One limitation of our method regarding the covariance matrix is that the computation of the \mathbf{X} and \mathbf{Y} matrices used in the covariance matrix is numerically expensive – they grow linearly with the multi-

pole range but as $n^4/4$ with the number n of different masks – and remains noisy. However, this method has the advantage of naturally taking care of partial sky coverage, without the need of inverting the mixing matrix to recover full-sky spectra, necessarily introducing numerical noise in the data. Devising a method that takes care of partial sky coverage whilst incorporating all relevant non-Gaussian terms will be an important task for future surveys (Lacasa et al. 2016).

Finally, the non-linear power spectrum of the matter density field suffers from theoretical uncertainties (Baldauf et al. 2016). With our choice of multipole ranges, we do not explore scales smaller than the non-linear transition scale (around $k_{\text{nl}} \sim 0.1 h/\text{Mpc}$), making our constraints robust to these uncertainties. In particular, the suppression of power due to massive neutrinos (Lesgourgues & Pastor 2006) and the contribution of baryonic and feedback processes (Leauthaud et al. 2017) at these scales will certainly be an important theoretical issue for future surveys.

6 CONCLUSION

Cosmological experiments carried out in the last few decades have enabled the construction of the Λ CDM model. In this picture, CDM drives the formation of the large-scale structure of the Universe and dark energy fuels the recent accelerated expansion. The combination of independent observations, such as the map of the anisotropies of the cosmic microwave background, distances of type Ia supernovae and the measurement of the scale of the baryon acoustic oscillations, have set constraints on the content of the Universe. However, the analysis of currently available data cannot distinguish between various models of dark matter and dark energy. Going further and deciphering the nature of these components requires better constraints, and thus, more information. To this end, deep galaxy surveys – such as LSST, Euclid and WFIRST – and CMB imagers – such as CMB-S4 and the Simons Observatory – with wide sky coverage and high resolution are currently under development. In the coming decade, they will probe the matter density field with ground-breaking precision and significantly increase the amount of cosmological information. Independent cosmological analyses have a strong potential to reveal new science, but model comparison will rely on exhausting the cosmological information held in the measurements of different cosmic probes and all their cross-correlations. In other words, a joint analysis of these probes is required.

In this paper, we have presented a detailed joint analysis of currently available data combining CMB measurements from the Planck satellite and LSS observations from the SDSS-III/BOSS spectroscopic survey. To this end, we developed a general framework in `NumCosmo` to compute and analyse the auto and cross correlations between an arbitrary number of cosmological probes. In particular, we applied our framework to analyse CMB lensing and galaxy clustering at once by measuring auto and cross angular power spectra. In Section 5.2.1, we showed how including cross-correlation information – present in the data – improves constraints on cosmological parameters and decreases the statistical errors, for example, by 10% for $\ln 10^{10} A_s$ and 20% for ω_c (when other parameters are fixed). This highlights the fact that ignoring part of the cosmological information (in this case, the

cross-correlations) could lead to inaccurate posterior distributions of the parameters.

Next, we included CMB temperature and carried out three different MCMC analyses, the first using only CMB temperature anisotropies (“CMB TT ”), then adding CMB lensing (“CMB TT + CMB lensing”) and finally the joint analysis per se (“CMB TT + CMB lensing \otimes LSS”). We compared the performance of these analyses for the base, 6-parameter, flat Λ CDM model, and then explored constraints on the mass of neutrinos and the DE equation of state, constraining four statistical models (see Figures 16, 18 and 20). As expected, constraints from the joint analysis are stronger than those obtained from CMB data only, in all cases. Because of the sensitivity of galaxy clustering and the CMB lensing-galaxy cross-correlations to m_ν and w , we were able to study extended models and constrain up to eight cosmological parameters at once (that is, H_0 , ω_b , ω_c , A_s , n_s , z_{re} , m_ν and w).

The joint analysis proves effective in doing so and yields the best constraints. This can be understood as the result of the strong correlations observed between galaxy clustering biases and some cosmological parameters, in particular H_0 and w . As a result, we observe the breaking of several degeneracies and significantly better constraints for various parameters, although this depends upon exactly which parameters are constrained and which are assumed to be fixed. A downside is that future surveys will have to measure these biases with great precision in order to be able to pin down the values of these parameters and to constrain a possible time dependence of dark energy. Interestingly, if we used a value of $H_0 = 72 \text{ km/s/Mpc}$ consistent with distance measurements from type Ia supernovae, then our constraints would favour a value of the DE equation of state of $w \sim -1.1$, *i.e.* a phantom dark energy, which is disfavoured by theoretical considerations. Finally, we also obtained upper limits on the total mass of neutrinos of 0.29 eV [68%] as a result of its impact on galaxy clustering at small scale. This is similar to limits obtained with other analyses.

In this work, we have used spectroscopic observations of galaxies and quasars, insulating us from uncertainties inherent to photometric redshifts. Similar work was done by Nicola et al. (2016) with photometric data from the SDSS, albeit constraining fewer parameters. However, the trade-off between the precision of redshifts and the much larger number of galaxies observed by future deep surveys like LSST could potentially lead to even better results. Moreover, imaging surveys can detect cosmic shear, a powerful probe of dark energy, by measuring distortions in the shapes of galaxies. Combining CMB lensing, galaxy lensing and galaxy clustering in a joint analysis is a promising avenue for cosmological parameters estimation.

Finally, in this near-future scenario of large amounts of data and joint analyses (including cross-correlations), we will be able to study different cosmological models emerging from different theories of gravity, such as effective field theories of dark energy (Gleyzes et al. 2016) or non-local gravity (Dirian et al. 2016), and hopefully start to distinguish and rule out some models with strong statistical significance.

ACKNOWLEDGEMENTS

CD would like to thank David Spergel and Emmanuel Schaan for useful comments and the opportunity to present a preliminary version of this work, Dhiraj Hazra for useful comments on the manuscript, Martin Kunz, Fabien Lacasa and Michele Maggiore for interesting discussions.

MPL received support from the National Council for Scientific and Technological Development - Brazil (CNPq grant 202131/2014-9 and PCI/MCTIC/CBPF program), and from the Labex ENIGMASS.

SDPV acknowledges the financial support from CNPq (PCI/MCTIC/CBPF program) and BELSPO non-EU postdoctoral fellowship.

Funding for SDSS-III has been provided by the Alfred P. Sloan Foundation, the Participating Institutions, the National Science Foundation, and the U.S. Department of Energy Office of Science. The SDSS-III web site is <http://www.sdss3.org/>.

SDSS-III is managed by the Astrophysical Research Consortium for the Participating Institutions of the SDSS-III Collaboration including the University of Arizona, the Brazilian Participation Group, Brookhaven National Laboratory, Carnegie Mellon University, University of Florida, the French Participation Group, the German Participation Group, Harvard University, the Instituto de Astrofísica de Canarias, the Michigan State/Notre Dame/JINA Participation Group, Johns Hopkins University, Lawrence Berkeley National Laboratory, Max Planck Institute for Astrophysics, Max Planck Institute for Extraterrestrial Physics, New Mexico State University, New York University, Ohio State University, Pennsylvania State University, University of Portsmouth, Princeton University, the Spanish Participation Group, University of Tokyo, University of Utah, Vanderbilt University, University of Virginia, University of Washington, and Yale University.

REFERENCES

- Abazajian K. N., et al., 2016, arXiv, p. arXiv:1610.02743
Allison R., et al., 2015, *Mon. Not. R. Astron. Soc.*, 451, 849
Alonso D., Ferreira P. G., 2015, *Phys. Rev. D*, 92, 063525
Alonso D., Bull P., Ferreira P. G., Maartens R., Santos M. G., 2015, *ApJ*, 814, 145
Baldauf T., Mirbabayi M., Simonović M., Zaldarriaga M., 2016
Baxter E. J., et al., 2016, arXiv, p. arXiv:1602.07384
Bianchini F., et al., 2015, *ApJ*, 802, 64
Bianchini F., et al., 2016, *ApJ*, 825, 24
Bleem L. E., et al., 2012, *ApJ*, 753, L9
Bonvin C., Durrer R., 2011, *Phys. Rev. D*, 84, 063505
Bonvin V., et al., 2017, *Mon. Not. R. Astron. Soc.*, 465, 4914
Boughn S. P., Crittenden R. G., Turok N. G., 1998, *New Astronomy*, 3, 275
Bovy J., et al., 2011, *ApJ*, 729, 141
Brooks S. P., Gelman A., 1998, *Journal of computational and graphical statistics*, 7, 434
Brown M. L., Castro P. G., Taylor A. N., 2005, *Mon. Not. R. Astron. Soc.*, 360, 1262
Cabr   A., Gazta  aga E., Manera M., Fosalba P., Castander F., 2006, *MNRAS*, 372, L23
Campagne J. E., Neveu J., Plaszczyński S., 2017
Chisari N. E., Dvorkin C., 2013, *J. Cosmol. Astropart. Phys.*, 2013, 029
Crittenden R. G., Turok N., 1996, *Phys. Rev. Lett.*, 76, 575
Dawson K. S., et al., 2013, *Astron. J.*, 145, 10
DiPompeo M. A., Myers A. D., Hickox R. C., Geach J. E., Holder G., Hainline K. N., Hall S. W., 2015, *Mon. Not. R. Astron. Soc.*, 446, 3492
Dias Pinto Vitenti S., Penna-Lima M., 2014, *Astrophysics Source Code Library*, p. ascl:1408.013
Dirian Y., Foffa S., Kunz M., Maggiore M., Pettorino V., 2016, *J. Cosmol. Astropart. Phys.*, 2016, 068
Doux C., Schaan E., Aubourg E., Ganga K., Lee K.-G., Spergel D. N., Tr  guer J., 2016, *Phys. Rev. D*, 94, 103506
Doux C., Penna-Lima M., Vitenti S. D. P., 2017, in prep.
Efstathiou G., 2004, *Mon. Not. R. Astron. Soc.*, 349, 603
Eftekharzadeh S., et al., 2015, *Mon. Not. R. Astron. Soc.*, pp 2780–2799
Fornengo N., Perotto L., Regis M., Camera S., 2015, *ApJ*, 802, L1
Fosalba P., Gazta  aga E., Castander F. J., 2003, *ApJ*, 597, L89
Geach J. E., et al., 2013, *ApJ*, 776, L41
Gelman A., Rubin D. B., 1992, *Statist. Sci.*, 7, 457
Giannantonio T., et al., 2016, *Mon. Not. R. Astron. Soc.*, 456, 3213
Gil-Mar  n H., Percival W. J., Verde L., Brownstein J. R., Chuang C.-H., Kitaura F.-S., Rodr  guez-Torres S. A., Olmstead M. D., 2016, *Mon. Not. R. Astron. Soc.*, pp 1757–1788
Gleyzes J., Langlois D., Mancarella M., Vernizzi F., 2016, *J. Cosmol. Astropart. Phys.*, 2016, 056
Goodman J., Weare J., 2010, *CAMCoS*, 5, 65
G  rski K. M., Hivon E., Banday A. J., Wandelt B. D., Hansen F. K., Reinecke M., Bartelmann M., 2005, *ApJ*, 622, 759
Hajian A., Battaglia N., Spergel D. N., Bond J. R., Pfrommer C., Sievers J. L., 2013, *J. Cosmol. Astropart. Phys.*, 11, 064
Hand N., et al., 2012, *Phys. Rev. Lett.*, 109, 041101
Hand N., et al., 2015, *Phys. Rev. D*, 91, 062001
Harnois-D  raps J., et al., 2016, arXiv, p. arXiv:1603.07723
Heidelberger P., Welch P. D., 1981, *Commun. ACM*, 24, 233
Heidelberger P., Welch P. D., 1983, *Oper. Res.*, 31, 1109
Hildebrandt H., et al., 2016, *Mon. Not. R. Astron. Soc.*, 465, 1454
Hill J. C., Spergel D. N., 2014, *J. Cosmol. Astropart. Phys.*, 02, 030
Hirata C. M., Ho S., Padmanabhan N., Seljak U., Bahcall N. A., 2008, *Phys. Rev. D*, 78, 043520
Hivon E., G  rski K. M., Netterfield C. B., Crill B. P., Prunet S., Hansen F., 2002, *ApJ*, 567, 2
Ho S., Hirata C., Padmanabhan N., Seljak U., Bahcall N., 2008, *Phys. Rev. D*, 78, 043519
Ho S., et al., 2012, *ApJ*, 761, 14
Hui L., Gazta  aga E., LoVerde M., 2007, *Phys. Rev. D*, 76, 103502
Hurvich C. M., Tsai C.-L., 1989, *Biometrika*, 76, 297
Jain B., Seljak U., White S., 2000, *ApJ*, 530, 547
Jain B., et al., 2015
Kirk D., et al., 2016, *Mon. Not. R. Astron. Soc.*, 459, 21
Krause E., Eifler T., 2016
Kwan J., et al., 2017, *MNRAS*, 464, 4045
LSST Science Collaborations and LSST Project et al., 2009, arXiv, p. arXiv:0912.0201
Lacasa F., Lima M., Aguen   M., 2016, arXiv, p. arXiv:1612.05958
Lamarre J. M., et al., 2010, *A&A*, 520, A9
Laurent P., et al., 2016, *J. Cosmol. Astropart. Phys.*, 11, 060
Laurent P., et al., 2017
Leauthaud A., et al., 2017, *Mon. Not. R. Astron. Soc.*, 467, 3024
Lesgourgues J., 2011, preprint, (arXiv:1104.2932)
Lesgourgues J., Pastor S., 2006, *Physics Reports*, 429, 307
Lesgourgues J., Tram T., 2014, *J. Cosmology Astropart. Phys.*, 9, 032

Lesgourgues J., Mangano G., Miele G., Pastor S., 2009, *Neutrino Cosmology*. Cambridge University Press, Cambridge, doi:10.1017/CBO9781139012874, <http://ebooks.cambridge.org/ref/id/CBO9781139012874>

Levi M., et al., 2013

Lewis A., Challinor A., 2006, *Phys. Rep.*, **429**, 1

Lewis A., Challinor A., Lasenby A., 2000, *ApJ*, **538**, 473

Limber D. N., 1953, *ApJ*, **117**, 134

Liu J., Ortiz-Vazquez A., Hill J. C., 2016, *Phys. Rev. D*, **93**, 103508

LoVerde M., Afshordi N., 2008, *Phys. Rev. D*, **78**, 123506

Mandolesi N., et al., 2010, *A&A*, **520**, A3

Moura-Santos E., Carvalho F. C., Penna-Lima M., Novaes C. P., Wuensche C. A., 2016, *ApJ*, **826**, 121

Nicola A., Refregier A., Amara A., 2016, *Phys. Rev. D*, **94**, 083517

Olive K. A., 2014, *Chinese Physics C*, **38**, 090001

Padmanabhan N., et al., 2007, *Mon. Not. R. Astron. Soc.*, **378**, 852

Palanque-Delabrouille N., et al., 2015, *J. Cosmol. Astropart. Phys.*, **02**, 045

Pâris I., et al., 2017, *A&A*, **597**, A79

Pearson R., Zahn O., 2014, *Phys. Rev. D*, **89**, 043516

Peiris H. V., Spergel D. N., 2000a, *ApJ*, **540**, 605

Peiris H. V., Spergel D. N., 2000b, *ApJ*, **540**, 605

Penna-Lima M., Makler M., Wuensche C. A., 2014, *J. Cosmol. Astropart. Phys.*, **05**, 039

Pisanti O., Cirillo A., Esposito S., Iocco F., Mangano G., Miele G., Serpico P. D., 2008, *Computer Physics Communications*, **178**, 956

Planck Collaboration et al., 2014, *A&A*, **571**, A17

Planck Collaboration et al., 2016a, *A&A*, **594**, A1

Planck Collaboration et al., 2016b, *A&A*, **594**, A9

Planck Collaboration et al., 2016c, *A&A*, **594**, A10

Planck Collaboration et al., 2016d, *A&A*, **594**, A11

Planck Collaboration et al., 2016e, *A&A*, **594**, A13

Planck Collaboration et al., 2016f, *A&A*, **594**, A13

Planck Collaboration et al., 2016g, *A&A*, **594**, A15

Planck Collaboration et al., 2016h, *A&A*, **594**, A21

Planck Collaboration et al., 2016i, *A&A*, **594**, A22

Planck Collaboration et al., 2016j, *A&A*, **594**, A24

Plummer M., Best N., Cowles K., Vines K., 2006, *R News*, **6**, 7

Refregier A., Amara A., Kitching T. D., Rassat A., Scaramella R., Weller J., Consortium f. t. E. I., 2010

Reid B., et al., 2016, *Mon. Not. R. Astron. Soc.*, **455**, 1553

Rhodes J., et al., 2015, *Astroparticle Physics*, **63**, 42

Riess A. G., et al., 2016, *ApJ*, **826**, 56

Schaan E., Takada M., Spergel D. N., 2014, *Phys. Rev. D*, **90**, 123523

Schaan E., Krause E., Eifler T., Dore O., Miyatake H., Rhodes J., Spergel D. N., 2016a, arXiv, p. arXiv:1607.01761

Schaan E., et al., 2016b, *Phys. Rev. D*, **93**, 082002

Schlegel D. J., et al., 2009, arXiv, p. arXiv:0904.0468

Schruben L. W., 1982, *Operations Research*, **30**, 569

Scranton R., et al., 2005, *ApJ*, **633**, 589

Sherwin B. D., et al., 2012, *Phys. Rev. D*, **86**, 083006

Smith R. E., et al., 2003a, *MNRAS*, **341**, 1311

Smith R. E., et al., 2003b, *Mon. Not. R. Astron. Soc.*, **341**, 1311

Smith K. M., Zahn O., Dore O., 2007, *Phys. Rev. D*, **76**, 043510

Spergel D., et al., 2013

Suzuki A., et al., 2016, *J Low Temp Phys*, **184**, 805

Takahashi R., Sato M., Nishimichi T., Taruya A., Oguri M., 2012a, *ApJ*, **761**, 152

Takahashi R., Sato M., Nishimichi T., Taruya A., Oguri M., 2012b, *ApJ*, **761**, 152

Takeuchi Y., Ichiki K., Matsubara T., 2012, *Phys. Rev. D*, **85**, 043518

Vallinotto A., 2012, *ApJ*, **759**, 32

Vitenti S. D. P., Penna-Lima M., Doux C., 2017, in prep.

White M., et al., 2012, *Mon. Not. R. Astron. Soc.*, **424**, 933

APPENDIX A: X/Y MATRICES IN THE COVARIANCE

The \mathbf{X} and \mathbf{Y} matrices appearing in eq. (23) have the following analytical expressions (Brown et al. 2005),

$$\begin{aligned}\mathbf{X}_{\ell_1\ell_2}^{ABCD} &= \frac{1}{(2\ell_1+1)(2\ell_2+1)} \times \\ &\sum_{m_1m_2} \sum_{\ell_3m_3} \sum_{\ell_4m_4} W_{\ell_1\ell_3m_1m_3}^A \bar{W}_{\ell_2\ell_3m_2m_3}^B W_{\ell_2\ell_4m_2m_4}^C \bar{W}_{\ell_1\ell_4m_1m_4}^D \\ \mathbf{Y}_{\ell_1\ell_2}^{ABCD} &= \frac{1}{(2\ell_1+1)(2\ell_2+1)} \times \\ &\sum_{m_1m_2} \sum_{\ell_3m_3} \sum_{\ell_4m_4} W_{\ell_1\ell_3m_1m_3}^A \bar{W}_{\ell_2\ell_3m_2m_3}^C W_{\ell_2\ell_4m_2m_4}^B \bar{W}_{\ell_1\ell_4m_1m_4}^D,\end{aligned}\quad (\text{A1})$$

where the $W_{\ell\ell'mm'}^A$ describe the convolution of the mask ($\bar{W}_{\ell\ell'mm'}^A$ is its complex conjugate), *i.e.* if the field $A(\hat{\mathbf{n}})$ has full-sky spherical harmonics coefficients $A_{\ell m}$ and pseudo-coefficients $\tilde{A}_{\ell m}$ then

$$\tilde{A}_{\ell m} = \sum_{\ell'm'} W_{\ell\ell'mm'}^A A_{\ell'm'}.\quad (\text{A2})$$

These cannot be analytically computed and MC simulations are therefore required. We take advantage of the fact that eq. (23) is exact if initial full-sky spectra do not depend on ℓ and that they need not have physically relevant values. The algorithm then proceeds as follows. First, we generate sets of four correlated maps with generic constant input auto and cross spectra, which we mask by the four masks used in our analysis. We then compute the spectra of the masked maps, thus building a collection of estimated pseudo spectra $\{\tilde{C}_{\ell}^{AB,i}\}_i$ where i represents the simulation index. The empirical covariance of the set of pseudo spectra is finally computed. Knowing the input spectra, an estimate of $\mathbf{X}_{\ell\ell'}^{ABCD}$ and $\mathbf{Y}_{\ell\ell'}^{ABCD}$ can be obtained using eq. (23). In the case where $A = B$ or $C = D$ and only in this case, the terms in the square roots in eq. (23) are equal and $\mathbf{X}_{\ell\ell'}^{ABCD}$ and $\mathbf{Y}_{\ell\ell'}^{ABCD}$ cannot be distinguished, but for all the other cases, it requires two sets of simulations to disentangle them.

We estimate the error on the empirical covariance matrices by bootstrapping the pseudo spectra $\{\tilde{C}_{\ell}^{AB,i}\}_i$ and require that the ratio of the norms of the error matrix to that of the empirical covariance matrix is smaller than 1%, which in our analysis necessitated more than 200 000 simulations.

In the case where $A = B = C = D$, these matrices reduce to symmetrized mixing matrices

$$\mathbf{X}_{\ell\ell'}^{AAAA} = \mathbf{Y}_{\ell\ell'}^{AAAA} = \frac{1}{2\ell'+1} \mathbf{M}_{\ell\ell'}^{AA},\quad (\text{A3})$$

which allows for comparison and validation of the MC simulations (see Figure A1). We find percent-level agreement on the diagonal, with a decreasing precision when moving further away from the diagonal as numerical noise (at least four orders of magnitude smaller than the diagonal elements) starts dominating.

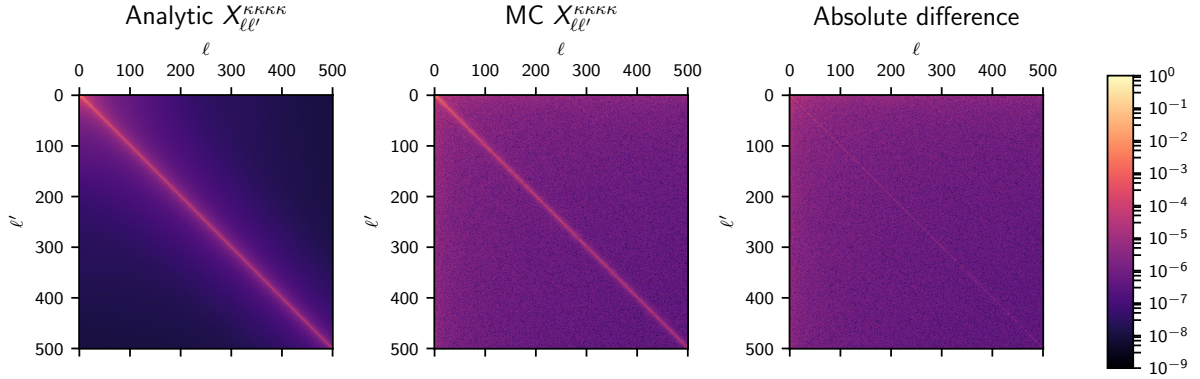


Figure A1. Comparison between the analytically-estimated (left panel) and simulation-estimated (middle panel) $\mathbf{X}_{\ell\ell'}^{KKKK}$ matrices in logarithmic scale. The absolute difference is shown on the right panel. The important features are well captured: the precision is better than 2% on the diagonal and degrades when getting further away from the diagonal. The middle panel shows that the far off-diagonal terms are dominated by numerical noise from our MC simulations, but are four orders of magnitudes smaller than the diagonal terms which are the most important, making it safe to use in the covariance matrix. The right panel shows the absolute difference.

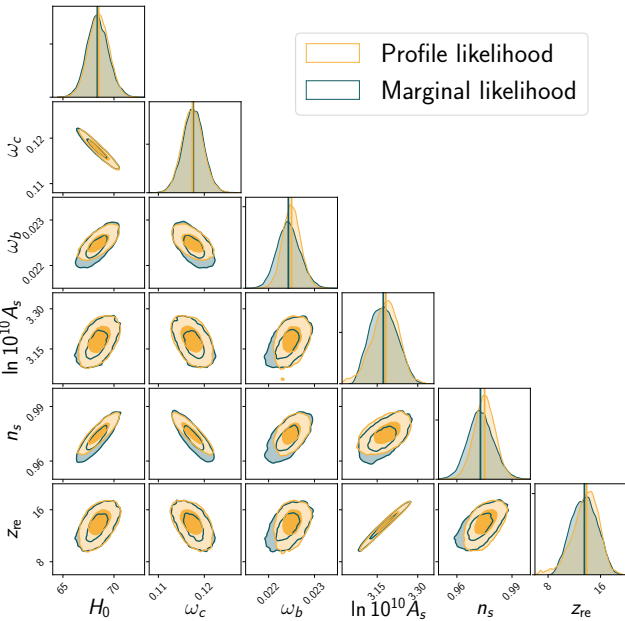


Figure B1. Comparison between the marginal likelihood (dark blue) and the profile likelihood (yellow). On the diagonal, the one-dimensional projections of the posterior distribution for each parameter is shown, the vertical lines corresponding to the mean value. For all the parameters, the difference between the means of the two distribution is much smaller than the statistical error. The standard deviations are also very close, with at worst a 10% decrease for n_s and ω_b .

APPENDIX B: PROFILE LIKELIHOOD

In order to accelerate our MCMC analyses, we choose to use the profile likelihood instead of the marginal likelihood for the nuisance parameters. The reason is that this procedure decreases the dimension of the parameter space and requires less calls to the Boltzmann code, resulting in an

overall faster convergence of the posterior distribution of the cosmological parameters. In practice, it amounts to compute the maximum likelihood estimator value of the nuisance parameters $\hat{\mathbf{A}}(\theta)$ for each set of cosmological parameters θ given the data (which is fast), and use this value in the likelihood. The posterior distribution is then given by $\mathcal{L}_{\text{profile}}(\theta | C_\ell^{TT}) \propto \mathcal{L}(C_\ell^{TT} | \theta, \hat{\mathbf{A}}(\theta))$ while the marginal likelihood is $\mathcal{L}_{\text{marginal}}(\theta | C_\ell^{TT}) \propto \int \mathcal{L}(C_\ell^{TT} | \theta, \mathbf{A}) d\mathbf{A}$. We demonstrate that it doesn't affect the results on the cosmological parameters by running two MCMC using only the CMB temperature power spectrum C_ℓ^{TT} , one performing the nuisance parameters subfitting procedure and the other using the standard marginalisation procedure. Figure B1 shows the posterior distribution in these two cases. The mean value of each parameter in both runs is shown in the one-dimensional plots on the diagonal. In all cases, the variation of the mean is much smaller than the statistical variance, and the standard deviation is at worst decreased by 15% in the profile likelihood (for n_s and ω_b , two parameters which are poorly constrained by the other observations), with almost no difference for the other parameters. This indicates that we can use either likelihoods indifferently. Since the profile likelihood method is faster overall, and that we don't have other nuisance parameters, we used it for all simulations in Section 5.2.2.

APPENDIX C: THE NUMCOSMO LIBRARY

In this section, we provide a short description of the Numerical Cosmology library (NumCosmo, available on GitHub¹⁸, Dias Pinto Vitenti & Penna-Lima (2014)). Apart from the crude data (observational maps), for which we used some Healpix functions to generate the observed pseudo- C_ℓ^{AB} values, as mentioned in Section 3, all other pieces of the pipeline made use of NumCosmo. For a complete description we refer

¹⁸ <https://github.com/NumCosmo/NumCosmo>

the reader to the references [Doux et al. \(2017\)](#) and [Vitenti et al. \(2017\)](#).

NumCosmo contains a comprehensive set of tools to compute cosmological observables and to perform statistical analysis. The library is written in C, but since it uses the **GObject** framework¹⁹, it is developed in a object-oriented fashion. Additionally, it has automatic bindings for every language that supports **GObject** introspection (*e.g.* Python, Ruby or Perl).

Physical models are implemented via the abstract class **NcmModel**. In particular, the Λ CDM and w CDM models, and all respective relevant functions are implemented in **NhICosmoDE** and child classes (such as **NhICosmoDEXcdm**), the primordial power spectrum is implemented in **NhIPrim**, the reionization model in **NhIReion**. Data objects deriving from the abstract class **NcmData** encapsulate the observations and implement likelihood functions. A general object for statistical analysis **NcmFit** is then built from the data and the model.

We first address the computation of the theoretical angular power spectrum, C_ℓ^{AB} (see eqs. (2) and (3)) and the likelihood function eq. (25):

(i) **NcXCor**: abstract class that comprises, among others, the methods to compute the auto and cross power spectra C_ℓ^{AA} and C_ℓ^{AB} .

(ii) **NcXCorLamberKernel**: abstract class of the type **NcmModel**²⁰ which defines the methods and general properties that a kernel $W^A(z)$ must implement, for any observable A . For instance, the computation of $W^A(z)$ at a given z and for a set of cosmological parameters, and the number of multipoles to be calculated.

- **NcXCorLamberKernelLensing**: implements the CMB lensing kernel, $W^{*CMB}(z)$ [eq. (6)].
- **NcXCorLamberKernelGal**: implements the galaxy kernel, $W^g(z)$ [eq. (8)].

(iii) **NcPowSpecMNL**: abstract class for the nonlinear matter power spectrum. Here we use the Halofit approach ([Smith et al. 2003a](#); [Takahashi et al. 2012a](#)), which we implemented in the **NcPowSpecMNLHaloFit** class. The linear matter power spectrum is calculated using **NcPowSpecMLCBE**, *i.e.*, the **NumCosmo** backend for the Cosmic Linear Anisotropy Solving System (CLASS) ([Lesgourgues 2011](#)).

(iv) **NcDataXCor**: this object builds the likelihood given by eq. (25), and it derives from **NcmDataGaussCov**, *i.e.*, the object that describes Gaussian-distributed data with non-diagonal covariance matrix.

Regarding the statistical analyses performed in this work, we made use of the following **NumCosmo** tools:

- (i) **NcmFit**: implements various interfaces with best-fit finders. In this work, we used the interface with the **NLOpt** library²¹ and the Nelder-Mead algorithm.
- (ii) **NcmFitMC**: implements the Monte Carlo analysis described in Section 4.2, using the same best-fit finder.

(iii) **NcmFitESMCMC**: implements the Ensemble Sampler Markov Chain Monte Carlo ([Goodman & Weare 2010](#)) analysis used throughout Section 5 of this paper. It requires an initial sampler **NcmMSetTransKern** and another sampler to move the walkers **NcmFitESMCMCWalker**.

Finally, we used CMB temperature data from Planck:

(i) **NcPlanckFICorTT**: implements Planck foreground and instrumental models for TT measurements.

(ii) **NcDataPlanckLKL**: implements the interface with Planck's likelihood codes **Plik** and **Commander**.

APPENDIX D: MCMC CONVERGENCE TESTS

In this work, we checked the convergence of the MCMC chains using three different methods, which we implemented closely following the R package **CODA** ([Plummer et al. 2006](#)). The first is the Multivariate Potential Scale Reduction Factor (MPSRF, [Gelman & Rubin 1992](#); [Brooks & Gelman 1998](#)). This method requires multiple chains, whose initial values must be over-dispersed in comparison with the posterior, and quantifies the mixing of the walkers by comparing the ensemble variance to the per-walker variance. Nevertheless, we do not know *a priori* the posterior and, for this reason, we may only guess what an over-dispersed distribution would be.

The second method is the Heidelberger-Welch diagnostic test ([Heidelberger & Welch 1981, 1983](#)), which consists in applying the Schruben stationarity test ([Schruben 1982](#)) to subsets of a chain to obtain one that satisfies the test for a given p -value. Since we are using an ensemble sampler, we can apply this test to each individual chain, or, more efficiently, to the ensemble mean of each parameter. We applied the individual approach only when the Markov chain presents convergence problems.

In the third approach, we calculated the autocorrelation time as proposed by [Goodman & Weare \(2010\)](#). However, in **NumCosmo**, instead of estimating the autocorrelation time directly from the autocorrelations, we fit an Auto Regressive (AR) model as in **CODA**. In the AR model fitting, we use the bias corrected Akaike Information Criterion (AICc) ([Hurvich & Tsai 1989](#)) to choose the best AR order to use for a given parameter in a chosen chain. This provides a less noisy estimate of the autocorrelation time than the direct inference from the autocorrelations (see [Goodman & Weare 2010](#)). The Effective Sample Size (ESS) is computed using that estimated autocorrelation time and provides an equivalent measure of the effective number of independent points in each chain. Finally, the variance of the sample mean of the parameters is given by the empirical variance of the sampled values divided by the ESS.

This paper has been typeset from a $\text{\TeX}/\text{\LaTeX}$ file prepared by the author.

¹⁹ <https://developer.gnome.org/gobject/stable/>

²⁰ Being a **NcmModel**, each implementation of **NcXCorLamberKernel** can define a respective set of parameters. For instance, the linear bias, $b(z)$, in eq. (8).

²¹ <http://ab-initio.mit.edu/nlopt>